

IEA Wind Task 46

Erosion of wind turbine blades

**A roadmap for producing
wind turbine blade coating
leading edge erosion
atlases: Preliminary results**

**Technical
Report**



iea wind

Technical Report

A roadmap for producing wind turbine blade coating leading edge erosion atlases: Preliminary results

**Prepared for the
International Energy Agency Wind Implementing Agreement**

Authors:

Sara C. Pryor, Cornell University (sp2279@cornell.edu)

Rebecca J. Barthelmie, Cornell University

Àsta Hannedóttir, DTU Wind

5 March 2025

IEA Wind TCP functions within a framework created by the International Energy Agency (IEA). Views, findings, and publications of IEA Wind do not necessarily represent the views or policies of the IEA Secretariat or of all its individual member countries. IEA Wind is part of IEA's Technology Collaboration Programme (TCP).

Purpose

Leading edge erosion (LEE) of wind turbine blades has been identified as a major factor in decreased wind turbine blade lifetimes and energy output over time. Accordingly, the International Energy Agency Wind Technology Collaboration Programme (IEA Wind TCP) has created the Task 46 to undertake cooperative research in the key topic of blade erosion. Participants in the task are given in Table 1.

The Task 46 under IEA Wind TCP is designed to improve understanding of the drivers of LEE, the geospatial and temporal variability in erosive events; the impact of LEE on the performance of wind plants and the cost/benefit of proposed mitigation strategies. Furthermore Task 46 seeks to increase the knowledge about erosion mechanics and the material properties at different scales, which drive the observable erosion resistance. Finally, the Task aims to identify the laboratory test setups which reproduce faithfully the failure modes observed in the field in the different protective solutions.

This report is a product of Work Package 2 **Climatic conditions driving blade erosion**.

The objectives of this report are to:

- Articulate and contrast methodologies used to produce erosion atlases
- Make recommendations regarding development of erosion atlases in the future that, if enacted, will enhance the fidelity/transparency and consistency of these products.

Table 1 IEA Wind Task 46 Participants.

Country	Contracting Party	Active Organizations
Belgium	The Federal Public Service of Economy, SMEs, Self-Employed and Energy	Engie
Canada	Natural Resources Canada	WEICan
Denmark	Danish Energy Agency	DTU (OA), Hempel, Ørsted A/S, PowerCurve, Siemens Gamesa Renewable Energy
Finland	Business Finland	VTT
Germany	Federal Ministry for Economic Affairs and Energy	Fraunhofer IWES, Covestro, Emil Frei (Freilacke), Nordex Energy SE, RWE, DNV, Mankiewicz, Henkel
Ireland	Sustainable Energy Authority of Ireland	South East Technology University, University of Galway, University of Limerick
Japan	New Energy and Industrial Technology Development Organization	AIST, Asahi Rubber Inc., Osaka University, Tokyo Gas Co.
Netherlands	Netherlands Enterprise Agency	TU Delft, TNO
Norway	Norwegian Water Resources and Energy Directorate	Equinor, University of Bergen, Statkraft
Spain	CIEMAT	CENER, Aerox, CEU Cardenal Herrera University, Nordex Energy Spain
United Kingdom	Offshore Renewable Energy Catapult	ORE Catapult, University of Bristol, Lancaster University, Imperial College London, Ilosta, Vestas
United States	U. S. Department of Energy	Cornell University, Sandia National Laboratories, 3M

Table of Contents

Purpose	3
1. Introduction	7
2. Erosion Atlas Methodologies	9
2.1 Meteorological input	10
2.2 Translating meteorological observations to blade coating lifetimes	11
3. Key Conclusions/Recommendations	12
4. References	13
Appendix A: An erosion atlas for the contiguous United States of America	17
Appendix B: An erosion atlas of Scandinavia	41

List of Figures

Figure 1 (a) Temporal and (b,c) spatial variability of precipitation.	8
Figure 2 Joint probability of mass-weighted mean diameter (D_m in mm) and rainfall rate (RR).	8
Figure 3 Summary of the methodology, and locations of currently operating wind turbines in CONUS and coating lifetime estimations.	17
Figure 4 Summary of the methodology and the coating lifetime estimates for Scandinavia.	41

Executive Summary

Wind turbine blade leading edge erosion (LEE) reduces electricity production and increases wind energy operation and maintenance costs. Degradation of the blade coating and resulting damage to the underlying blade structure is caused primarily by collisions of falling hydrometeors with rapidly rotating blades. Selection of optimal methods to extend coating lifetimes and/or make recommendations about use of mitigation options can be informed by information regarding the erosion characteristics in both space (location) and through time. Accordingly, erosion atlases are being developed to meet this need. This report provides examples of currently available erosion atlases, articulates and contrasts methodologies used to produce these erosion atlases and make recommendations to enhance the fidelity and consistency of future erosion atlases.

1. Introduction

Erosion of wind turbine blade coatings with subsequent exposure and erosion of the substrate is a cause of decreased aerodynamic performance and increased operations and maintenance costs (Pryor et al. 2024). The rate at which coating lifetimes are exhausted is highly variable in space and time due, at least in part, to variations in prevailing atmospheric conditions at locations where wind turbines are deployed.

The primary driver of leading edge erosion (LEE) at most locations is thought to be materials stresses caused by impacts from falling hydrometeors on rapidly rotating wind turbine blades. To the first order, when a liquid droplet impinges on a relatively flexible surface such as a wind turbine blade coating, compression of the liquid causes a (modified) Waterhammer pressure of a magnitude that depends on the closing velocity, the densities of the liquid and elastic coating plus the wave velocities sound in the liquid and coating (Keegan; Nash; Stack 2013). The impact first generates a surface compressional wave, then shear waves propagate into the material and Rayleigh waves are generated and propagate along the surface (Keegan; Nash; Stack 2013). More detailed modeling indicates that 3-dimensional dynamic pressure fields, like the impact force, also depend on the diameter (and shape) of droplet (Hoksbergen; Akkerman; Baran 2023; Pryor et al. 2024).

Accordingly, meteorological parameters of importance to blade coating lifetimes are:

- 1) Hydroclimate properties including precipitation rates (a measure of the depth of liquid water equivalent accumulation at the ground per time interval), the number size distribution of liquid hydrometeors (rain droplets) plus the occurrence and number size distribution of hailstones, and the fall velocities of the hydrometeors.
- 2) Wind speeds and hence wind turbine blade rotational speed.

The joint occurrence (or copula probabilities) of wind speed and precipitation (rates, hydrometeor size distributions plus the hydrometeor phase) are the critical determinants of materials stresses and thus coating lifetimes.

Precipitation properties such as occurrence, intensity and phase exhibit very high temporal and spatial variability (e.g. Figure 1) (Zhang and Wang 2021). As shown in Figure 1, when 4 years of 1-minute non-zero rainfall rate (RR) observations at a site in the U.S. Southern Great Plains are averaged to longer time intervals, event intensity is reduced. For this example, the maximum (75th percentile) precipitation intensity in a 1-minute period is $> 140 \text{ mmhr}^{-1}$ (1.8 mmhr^{-1}) while equivalent values for data averaged to 10-minute intervals are $< 80 \text{ mmhr}^{-1}$ (0.94 mmhr^{-1}). Data from a scanning Doppler RADAR in this same location also indicates very strong spatial gradients in RR and duration of precipitation (Figure 1b,c) particularly during periods with deep convection (Pryor et al. 2023; Zhou et al. 2024). Temporal and spatial variability of precipitation and wind speeds complicate accurate estimation of instantaneous and long-term blade coating erosion at the wind farm and wind turbine scales. A further confounding issue pertains to the relationship between precipitation intensity (or rainfall rates, RR) and hydrometeor size distribution. As shown by Figure 2, the representative (mass weighted mean) diameter of rain droplets tends to increase with RR, but there is substantial event-to-event variability in this relationship. Thus, there is no universally applicable equation to describe hydrometeor size distributions (HSD) as a function of prevailing rainfall rate (Dolan et al. 2018; Pryor et al. 2022).

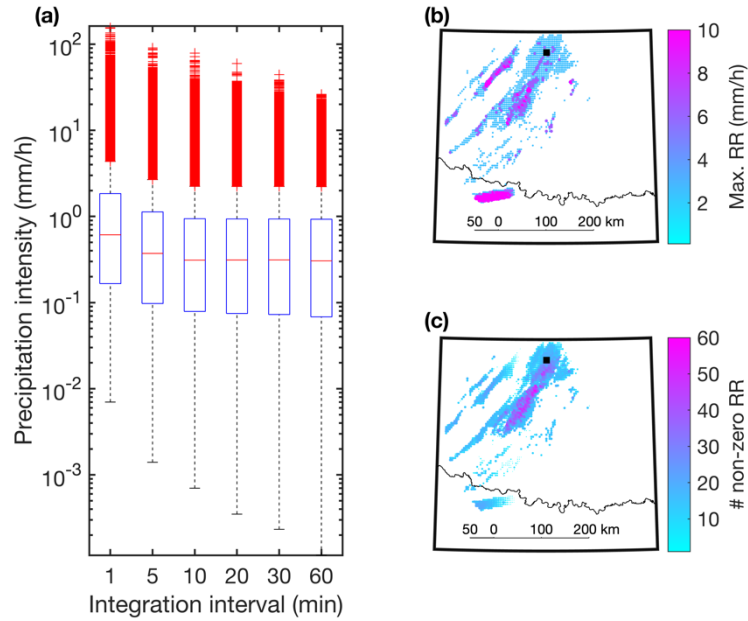


Figure 1 (a) Temporal and (b,c) spatial variability of precipitation.

(a) Boxplots of precipitation intensity (Rainfall Rate (RR) (mmhr^{-1})) as a function of the data integration (i.e. data averaging) period. Analyses of data from a site in the U.S. Southern Great Plains (black square presented in panel b). (b) Maximum precipitation intensity (mmhr^{-1}) based on ~ 5 -minute observations with a dual polarization scanning Doppler RADAR in Oklahoma City (Oklahoma/Texas state boundary shown by the thin black line) during 24th March 2024. Data are measured at high spatial resolution but are presented here on $\sim 4 \times 4$ km grid to aid legibility. The colorbar is also truncated to aid legibility (max RR in any grid cell is 25.4 mmhr^{-1}) (c) Number (out of 125) of all ~ 5 -minute measurement periods with non-zero precipitation.

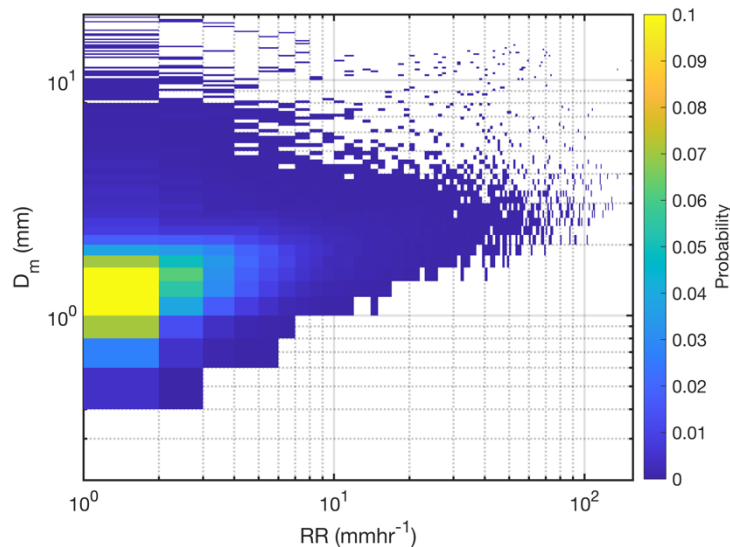


Figure 2 Joint probability of mass-weighted mean diameter (D_m in mm) and rainfall rate (RR).

RR and D_m are computed based on disdrometer measurements at the same site as Figure 1a. This site is located in the U.S. Southern Great Plains and is described in detail in Pryor et al. (2022). D_m is a metric used to describe the average (or representative) rain droplet diameter. It is computed as the ratio of the 3rd to the 4th moments of the measured droplet size

distribution: $D_m = \frac{M_4}{M_3}$ where the moments are given by $M_n = \sum_{i=1}^{NB} N(D_i) D_i^n \Delta D_i$. $N(D_i)$ is the number concentration in each diameter class (i). NB is the number of diameter classes. ΔD_i is the width of diameter class i, and D_i is the mean diameter of size class i.

Possible measures that can be employed to reduce rates of wind turbine blade leading edge erosion include:

- (i) Redesign of blades, use of more energy absorbing materials in coatings or reduction of manufacturing defects (Fæster et al. 2021; Frost-Jensen Johansen et al. 2021; Hinzmann et al. 2024; Mishnaevsky Jr et al. 2023; Pathak et al. 2023).
- (ii) Use of leading edge protection (LEP) products (Ansari et al. 2024; Herring et al. 2019; Katsivalis et al. 2022; Major et al. 2021; Sareen; Sapre; Selig 2014).
- (iii) Dynamical operation of wind turbines to reduce rotor speed during periods associated with high damage (i.e. intense precipitation at high operating wind speeds, when the blades are moving at their maximum rotational speed) (Bech; Hasager; Bak 2018; Letson and Pryor 2023).

Viability of these mitigation measures are critically reliant on joint probability distributions of wind speeds and hydroclimate properties plus market conditions all of which are likely to be to-some-degree location specific.

To help inform implementation of possible erosion mitigation measures, several activities have been undertaken to generate what will be referred to here as “wind turbine blade coating erosion atlases” (or erosion atlases). To varying degrees these atlases attempt to quantify:

- 1) The long-term spatial variability of coating lifetimes, and in some cases, also
- 2) The temporal variability in coating lifetime exhaustion at locations for which coating lifetimes have been quantified.

This report briefly summarizes recent research in this arena and provides two exemplar articles that demonstrate different methodological approaches to erosion atlas development. We conclude by identifying possible future research directions to enhance the utility and accuracy of these atlases.

2. Erosion Atlas Methodologies

Much of the research to date that has sought to derive estimates of wind turbine blade coating lifetimes has focused on the European continent and North America.

- Examples for Europe include; Danish Seas (Hasager et al. 2020), Scandinavia (Hannesdóttir et al. 2024), and the Netherlands (Bartolomé and Teuwen 2021).
- Examples for North America include; the United States of America (Letson; Barthelmie; Pryor 2020a; Letson; Barthelmie; Pryor 2020b; Pryor; Coburn; Barthelmie 2025).

A summary of existing erosion atlases is given below to highlight and contrast the range of methodologies being used in this research. Two specific examples of erosion atlases are presented in the appendices:

- Appendix A: contiguous United States of America (CONUS) (Pryor; Coburn; Barthelmie 2025)
- Appendix B: Scandinavia (Hannesdóttir et al. 2024).

These atlases employ different methodologies and data sets and are presented to provide exemplars of these products along with further detailed insights into critical assumptions and key properties of erosion atlases. The reader can download these erosion atlases at; <https://zenodo.org/records/14247620> and https://gitlab.windenergy.dtu.dk/astah/era5_erosion_atlas, respectively.

2.1 Meteorological input

A range of different meteorological data sets have been employed in the development of erosion atlases, including:

- 1) Reanalyses. A reanalysis dataset is a gridded product describing past meteorological (and climate) conditions generated by combining observations with numerical models to generate a consistent picture of atmospheric conditions. For further information, see the fact sheet generated by the European Centre for Medium-Range Weather Forecasts (ECMWF) available at: <https://www.ecmwf.int/en/about/media-centre/focus/2023/fact-sheet-reanalysis>. An example of an erosion atlas based on reanalysis products is given in Appendix B. Key advantages of using reanalysis products are that the output values are available on regular grids (e.g. ERA5 output is specified at a resolution of $\sim 30 \times 30$ km) and at regular time intervals and for a long time (frequently multiple decades). Disadvantages include that the fidelity of the reanalysis output is variable in space and time (and by meteorological parameter) due to the variations in availability and quality of observations used in the reanalysis workflow (Diniz and Todling 2020). Further, reanalysis products have an ‘effective resolution’ (i.e. a spatial scale where the amount of variance expressed is correct (Skamarock 2004) and thus processes and gradients are well reproduced) that is often many times the specified grid spacing (Cavalleri et al. 2024). Thus, gradients in meteorological parameters are under-sampled (i.e. the fields are too ‘smooth’). Further, the reanalysis output time step is often relatively long (e.g. 20 minutes or longer), thus high frequency variability in, for example, precipitation rates are under sampled.
- 2) Remote sensing data sets. Observations of both precipitation and wind speeds from individual ground-based remote sensing devices (e.g. dual-polarization scanning Doppler RADAR) have also been used to develop blade coating lifetimes (Letson; Barthelmie; Pryor 2020a; Letson; Barthelmie; Pryor 2020b). Key advantages of using RADAR data include availability of additional information regarding hail occurrence and properties. Disadvantages include that the wind speeds for wind turbine relevant heights are only available for a relatively narrow annulus around the station (and are of varying fidelity as a function of wind speed) and that the requirements for pre-processing of the observations are not inconsiderable. Further, although there are almost 150 such systems operating in CONUS, RADAR coverage in other countries may be more limited, thus the results are inhomogeneous in space and do not cover offshore areas. Multiple different gridded precipitation data sets based on satellite-borne sensors have also been developed (Pradhan et al. 2022; Sun et al. 2018). These include Global Precipitation Measurement (GPM) mission (IMERG) V07 Final Run dataset that contains 30-minute average precipitation rates (mm/hr) on a global $0.1^\circ \times 0.1^\circ$ grid (Huffman et al. 2020) and the Multi-Source Weighted-Ensemble Precipitation, version 2 (MSWEP V2) Global 3-Hourly 0.1° data set (Beck et al. 2019). The major disadvantage of these satellite products for erosion

atlas construction is the relatively coarse spatial resolution and long temporal averaging as well as recognized negative biases in intense precipitation. However, IMERG V07 Final Run greatly outperforms prior versions in terms of the capture of the upper percentiles of the precipitation probability distribution (Pryor et al. 2025). Use of satellite-based precipitation products for construction of erosion atlases relies upon integration with wind speeds from other sources (Badger et al. 2022).

- 3) In situ observations. Multiple erosion atlases have been developed based on in situ measurements from national operational meteorological networks (Bartolomé and Teuwen 2021; Hasager et al. 2020; Pryor; Coburn; Barthelmie 2025). An example of an erosion atlas based on in situ observations is given in Appendix A. Key advantages of using in situ measurements are that they are based on the best available descriptions of prevailing meteorology. Key disadvantages are that they are location specific and, even in places such as the USA where nearly 900 in situ Automated Surface Observing System (ASOS) stations with common instrumentation are available that report data with 5-minute frequency, some locations are not sampled. Further, wind speed measurements are taken at 10-m height in the ASOS network and thus are greatly below wind turbine hub-heights requiring vertical extrapolation. If a stipulation be placed that the available data include hydrometeor size (HSD) and phase information, the spatial representation drops dramatically to a very few sites and the data record duration is typically very limited (Letson and Pryor 2023; Pryor et al. 2022).
- 4) Mesoscale model output. A range of numerical weather prediction (NWP) models – e.g. the Weather Research and Forecasting model have been developed within the meteorological and climate communities. These models are initialized (i.e. started from) observations and then solve partial differential equations to make predictions of atmospheric conditions at future times. Erosion atlases based on NWP have been developed for parts of the North Sea and CONUS (Caboni and van Dalum 2024; Pryor et al. 2023). Key advantages of NWP-based erosion atlases are that these models (like those used to generate reanalysis products) discretize the atmosphere into grid boxes and generate output for each of those grid boxes. Thus, output is available with a common time and space scale throughout the simulation domain. Key disadvantages are that the output fidelity, particularly for rain precipitation intensity and phase, are highly dependent on model formulation (Pryor et al. 2023; Pryor et al. 2024) and that fidelity for these properties requires small grid spacing ($dx < 2$ km) thus performing simulations is computationally expensive and the resulting data volumes are substantial. Common with other datasets described herein, NWP models typically do not explicitly simulate precipitation HSD, and thus empirical HSD functions must be applied to simulation output HSD if the erosion methodology is predicated on size-resolved concentrations and fall velocities of hydrometeors.

2.2 Translating meteorological observations to blade coating lifetimes

A range of different methodologies have been employed to translate meteorological observations to coating lifetime estimates and/or a proxy thereof, including but not limited to:

- 1) Use of kinetic energy of impact between the falling hydrometeors and the rotating blades (Letson and Pryor 2023; Letson; Barthelmie; Pryor 2020a; Letson; Barthelmie; Pryor 2020b). In this approach a fundamental assumption

is invoked that the physical damage to a material caused by collisions scales, to the first order, with the kinetic energy of collisions. An advantage of this approach is the resulting assessment are ‘materials-neutral’ (i.e. there is no requirement for knowledge regarding the coating or substrate properties). Disadvantages include that the accumulated kinetic energy of impacts does not readily translate to a coating lifetime.

- 2) Use of the multi-layer Springer model (Herring et al. 2021; Hoksbergen; Akkerman; Baran 2022; Letson and Pryor 2023; Pryor; Coburn; Barthelmie 2025; Springer 1976; Springer and Baxi 1974; Springer; Yang; Larsen 1974) (see Appendix A for an example). This model uses material properties of the blade and coating to compute the number of impacts required for failure per unit area for a given hydrometeor diameter, closing velocity and impact angle. Via integration across these variables and then time, the model can be used to derive an accumulated distance to failure of the coating and the time required for onset of blade erosion. Example key advantages of this methodology are that the material properties are explicit in that they dictate key parameters in the model and can be readily changed if information is available regarding the coating or substrate. Example key disadvantages are that properties of actual materials being used within the wind energy industry are often held confidential and there is a need to employ an empirical hydrometeor size distribution conditioned on precipitation rate if measured HSD are not available.
- 3) Use of velocity- and number of impacts/impinged water relationships parameters from rain erosion testers (RET) (see Appendix B for an example). This approach relies upon empirical fitting of results from accelerated tests performed in whirling arm, pulsating jet, and rubber ball testers (Fujisawa et al. 2023). Experimental results are usually summarized in a V-N curve for erosion initiation, where V denotes the impact velocity of the droplet and N denotes the number of impacts (or H denotes the depth of impinged water for failure). Major advantages of this approach include that it is very computationally efficient since only two parameters from the RET are applied to precipitation rates to derive damage accumulation. Further, RET experiments can be conducted for actual materials used in wind turbine blades and/or LEP products (Kinsley et al. 2025). Major disadvantages of this approach include that the RET conditions do not fully replicate real atmospheric conditions (e.g. most RET experiments have employed continuous operation and at very high closing velocities and hence results need to be extrapolated to actual conditions, e.g. lower closing velocities), the exact V-N or V-H power law coefficients are uncertain and may vary across different experiments, the material properties of the sample are not always known/reported and thus may not reflect the actual coating/be repeatable and most analyses have employed (implicitly) an assumption of a single uniform droplet diameter irrespective of the precipitation intensity.

3. Key Conclusions/Recommendations

Increasingly sophisticated data sets and tools are being employed to develop geospatially, and to some degree, temporally explicit assessments of wind turbine blade coating lifetimes. However, the results from different studies are highly dependent on the meteorological data sets employed and the methodology used to

translate meteorology to coating lifetimes. Further, most erosion atlases implicitly or explicitly neglect the role of hail as a damage vector, although there is evidence that in parts of the globe that are subject to deep convection (thunderstorms), hail maybe be an important, or event dominant, source of coating damage (Letson; Barthelmie; Pryor 2020a).

Future research on development of wind turbine blade coating erosion atlases could/should:

- 1) Explicitly address sensitivity of atlases to end-to-end methodological decisions including assumptions regarding the HSD (and their fall velocities) and should increasingly integrate size-dependent hydrometeor measurements where possible.
- 2) Include explicit treatment of hail due to evidence that materials response to hail impacts may greatly exceed that for liquid droplets (Heymsfield et al. 2018; Keegan; Nash; Stack 2013; Kim and Kedward 2000; Letson; Barthelmie; Pryor 2020a; Macdonald and Stack 2021; Zhu et al. 2022).
- 3) Use a standardized wind turbine model for assessment of tip speeds and hence closing velocities between falling hydrometeors and rotating blades. This will aid in making quantitative comparison of relative erosion intensity across space (i.e. between different parts of the globe).
- 4) Use measured/modeled wind speeds close to wind turbine hub-heights to derive time varying blade tip-speeds. Many of the erosion atlases described above implicitly or explicitly vertically extrapolate wind speeds from their original measurement or nominal modeled height to wind turbine hub-heights. Use of wind speeds at/close to actual hub-heights will decrease error/uncertainty.
- 5) Include explicit assessment of the time-variability in the occurrence of damage.

These measures will enhance the utility and robustness of erosion atlases.

4. References

- Ansari, Q. M., F. Sánchez, L. Mishnaevsky Jr, and T. M. Young, 2024: Evaluation of offshore wind turbine blades coating thickness effect on leading edge protection system subject to rain erosion. *Renewable Energy*, **226**, 120378, doi: 10.1016/j.renene.2024.120378.
- Badger, M., H. Zuo, Á. Hannesdóttir, A. Owda, and C. Hasager, 2022: Lifetime prediction of turbine blades using global precipitation products from satellites. *Wind Energy Science*, **7**, 2497-2512.
- Bartolomé, L., and J. Teuwen, 2021: Methodology for the energetic characterisation of rain erosion on wind turbine blades using meteorological data: A case study for The Netherlands. *Wind Energy*, **24**, 686-698.
- Bech, J. I., C. B. Hasager, and C. Bak, 2018: Extending the life of wind turbine blade leading edges by reducing the tip speed during extreme precipitation events. *Wind Energy Science*, **3**, 729-748.
- Beck, H. E., E. F. Wood, M. Pan, C. K. Fisher, D. G. Miralles, A. I. Van Dijk, T. R. McVicar, and R. F. Adler, 2019: MSWEP V2 global 3-hourly 0.1 precipitation: methodology and quantitative assessment. *Bulletin of the American Meteorological Society*, **100**, 473-500.

- Caboni, M., and G. van Dalum, 2024: Developing an atlas of rain-induced leading edge erosion for wind turbine blades in the Dutch North Sea. *Wind Energy Science Discussions*, **2024**, 1-25, <https://doi.org/10.5194/wes-2024-5174>.
- Cavalleri, F., and Coauthors, 2024: Multi-scale assessment of high-resolution reanalysis precipitation fields over Italy. *Atmospheric Research*, **312**, 107734, <https://doi.org/10.1016/j.atmosres.2024.107734>.
- Diniz, F. L., and R. Todling, 2020: Assessing the impact of observations in a multi-year reanalysis. *Quarterly Journal of the Royal Meteorological Society*, **146**, 724-747.
- Dolan, B., B. Fuchs, S. Rutledge, E. Barnes, and E. Thompson, 2018: Primary modes of global drop size distributions. *Journal of the Atmospheric Sciences*, **75**, 1453-1476.
- Fæster, S., N. F. J. Johansen, L. Mishnaevsky Jr, Y. Kusano, J. I. Bech, and M. B. Madsen, 2021: Rain erosion of wind turbine blades and the effect of air bubbles in the coatings. *Wind Energy*, **24**, 1071-1082.
- Frost-Jensen Johansen, N., L. Mishnaevsky Jr, A. Dashtkar, N. A. Williams, S. Fæster, A. Silvello, I. G. Cano, and H. Hadavinia, 2021: Nanoengineered graphene-reinforced coating for leading edge protection of wind turbine blades. *Coatings*, **11**, 1104, doi: 1110.3390/coatings11091104.
- Fujisawa, N., N. F.-J. Johansen, T. Yamagata, K. Fujisawa, and M. Tanaka, 2023: A Review and Comparative Study of Uncertainty in Rain Erosion Testers for Wind Turbine Blades. *Journal of Flow and Energy*, **1**, 1-15.
- Hannesdóttir, Á., S. T. Kral, J. Reuder, and C. B. Hasager, 2024: Rain erosion atlas for wind turbine blades based on ERA5 and NORA3 for Scandinavia. *Results in Engineering*, **22**, 102010, <https://doi.org/10.1016/j.rineng.2024.102010>.
- Hasager, C., F. Vejen, J. Bech, W. Skrzypiński, A.-M. Tilg, and M. Nielsen, 2020: Assessment of the rain and wind climate with focus on wind turbine blade leading edge erosion rate and expected lifetime in Danish Seas. *Renewable Energy*, **149**, 91-102.
- Herring, R., K. Dyer, F. Martin, and C. Ward, 2019: The increasing importance of leading edge erosion and a review of existing protection solutions. *Renewable and Sustainable Energy Reviews*, **115**, 109382 doi: 10.1016/j.rser.2019.109382.
- Herring, R., L. Domenech, J. Renau, A. Šakalytė, C. Ward, K. Dyer, and F. Sánchez, 2021: Assessment of a wind turbine blade erosion lifetime prediction model with industrial protection materials and testing methods. *Coatings*, **11**, 767, doi: 10.3390/coatings11070767.
- Heymsfield, A., M. Szakáll, A. Jost, I. Giammanco, and R. Wright, 2018: A comprehensive observational study of graupel and hail terminal velocity, mass flux, and kinetic energy. *Journal of the Atmospheric Sciences*, **75**, 3861-3885.
- Hinzmann, C., N. F.-J. Johansen, C. B. Hasager, and B. Holst, 2024: Towards greener wind power: Nanodiamond-treated flax fiber composites outperform standard glass fiber composites in impact fatigue tests. *Composites Part A: Applied Science and Manufacturing*, **186**, 108342, <https://doi.org/10.1016/j.compositesa.2024.108342>.
- Hoksbergen, N., R. Akkerman, and I. Baran, 2022: The Springer model for lifetime prediction of wind turbine blade leading edge protection systems: A review and sensitivity study. *Materials*, **15**, 1170, doi: 10.3390/ma15031170.
- Hoksbergen, T., R. Akkerman, and I. Baran, 2023: Rain droplet impact stress analysis for leading edge protection coating systems for wind turbine blades.

- Renewable Energy*, **218**, 119328, <https://doi.org/10.1016/j.renene.2023.119328>.
- Huffman, G. J., and Coauthors, 2020: Integrated multi-satellite retrievals for the global precipitation measurement (GPM) mission (IMERG). *Satellite precipitation measurement: Volume 1*, 343-353.
- Katsivalis, I., A. Chanteli, W. Finnegan, and T. M. Young, 2022: Mechanical and interfacial characterisation of leading-edge protection materials for wind turbine blade applications. *Wind Energy*, **25**, 1758-1774.
- Keegan, M. H., D. Nash, and M. Stack, 2013: On erosion issues associated with the leading edge of wind turbine blades. *Journal of Physics D: Applied Physics*, **46**, 383001, doi: 10.1088/0022-3727/46/38/383001.
- Kim, H., and K. T. Kedward, 2000: Modeling hail ice impacts and predicting impact damage initiation in composite structures. *AIAA journal*, **38**, 1278-1288.
- Kinsley, P., S. Porteous, S. Jones, P. Subramanian, O. Campo, and K. Dyer, 2025: Limitations of Standard Rain Erosion Tests for Wind Turbine Leading Edge Protection Evaluation. *Wind*, **5**, 3 doi: 10.3390/wind5010003.
- Letson, F., and S. C. Pryor, 2023: From Hydrometeor Size Distribution Measurements to Projections of Wind Turbine Blade Leading Edge Erosion. *Energies*, **5**, 3906, <https://doi.org/10.3390/en16093906>.
- Letson, F., R. J. Barthelmie, and S. C. Pryor, 2020a: RADAR-derived precipitation climatology for wind turbine blade leading edge erosion. *Wind Energy Science*, **5**, 331-347.
- Letson, F. W., R. J. Barthelmie, and S. C. Pryor, 2020b: Sub-regional variability in wind turbine blade leading-edge erosion potential. *Journal of Physics Conference Series*, **1618**, 032046, doi: 10.1088/1742-6596/1618/3/032046.
- Macdonald, J., and M. Stack, 2021: Some thoughts on modelling hail impact on surfaces. *Journal of Bio-and Tribo-Corrosion*, **7**, 1-7, doi: 10.1007/s40735-020-00458-4.
- Major, D., J. Palacios, M. Maughmer, and S. Schmitz, 2021: Aerodynamics of leading-edge protection tapes for wind turbine blades. *Wind Engineering*, **45**, 1296-1316.
- Mishnaevsky Jr, L., A. Tempelis, N. Kuthe, and P. Mahajan, 2023: Recent developments in the protection of wind turbine blades against leading edge erosion: Materials solutions and predictive modelling. *Renewable Energy*, **215**, 118966, doi: 10.1016/j.renene.2023.118966.
- Pathak, S. M., V. P. Kumar, V. Bonu, L. Mishnaevsky Jr, R. Lakshmi, P. Bera, and H. C. Barshilia, 2023: Development of cellulose-reinforced polyurethane coatings: A novel eco-friendly approach for wind turbine blade protection. *Energies*, **16**, 1730, <https://doi.org/10.3390/en16041730>.
- Pradhan, R. K., and Coauthors, 2022: Review of GPM IMERG performance: A global perspective. *Remote Sensing of Environment*, **268**, 112754, <https://doi.org/10.1016/j.rse.2021.112754>.
- Pryor, S. C., J. J. Coburn, and R. J. Barthelmie, 2025: Spatiotemporal Variability in Wind Turbine Blade Leading Edge Erosion. *Energies*, **18**, 425, <https://doi.org/10.3390/en18020425>.
- Pryor, S. C., F. Letson, T. Shepherd, and R. J. Barthelmie, 2023: Evaluation of WRF simulation of deep convection in the US Southern Great Plains. *Journal of Applied Meteorology and Climatology*, **62**, 41-62.

- Pryor, S. C., R. J. Barthelmie, X. Zhou, and G. J. Huffman, 2025: Re-examining urban rainfall enhancement over North America. *Environmental Research Letters*, **20**, 034035, <https://doi.org/10.1088/1748-9326/adb507>.
- Pryor, S. C., and Coauthors, 2022: Atmospheric Drivers of Wind Turbine Blade Leading Edge Erosion: Review and Recommendations for Future Research. *Energies*, **15**, 8553, <https://doi.org/10.3390/en15228553>.
- Pryor, S. C., and Coauthors, 2024: Prioritizing Research for Enhancing the Technology Readiness Level of Wind Turbine Blade Leading-Edge Erosion Solutions. *Energies*, **17**, 6285, <https://doi.org/10.3390/en17246285>.
- Sareen, A., C. A. Sapre, and M. S. Selig, 2014: Effects of leading edge erosion on wind turbine blade performance. *Wind Energy*, **17**, 1531-1542.
- Skamarock, W. C., 2004: Evaluating mesoscale NWP models using kinetic energy spectra. *Monthly Weather Review*, **132**, 3019-3032, doi: 10.1175/mwr2830.1.
- Springer, G. S., 1976: *Erosion by liquid impact*. John Wiley and Sons, New York, NY, 278 pp.
- Springer, G. S., and C. B. Baxi, 1974: A model for rain erosion of homogeneous materials. *Erosion, Wear, and Interfaces with Corrosion*, 106-124.
- Springer, G. S., C.-I. Yang, and P. S. Larsen, 1974: Analysis of rain erosion of coated materials. *Journal of Composite Materials*, **8**, 229-252.
- Sun, Q., C. Miao, Q. Duan, H. Ashouri, S. Sorooshian, and K. L. Hsu, 2018: A review of global precipitation data sets: Data sources, estimation, and intercomparisons. *Reviews of Geophysics*, **56**, 79-107.
- Zhang, Y., and K. Wang, 2021: Global precipitation system size. *Environmental Research Letters*, **16**, 054005.
- Zhou, X., F. Letson, P. Crippa, and S. C. Pryor, 2024: Urban effect on precipitation and deep convective systems over Dallas-Fort Worth. *Journal of Geophysical Research: Atmospheres*, **129**, e2023JD039972, <https://doi.org/10.1029/2023JD039972>.
- Zhu, X., X. Fu, L. Liu, K. Xu, G. Luo, Z. Zhao, and W. Chen, 2022: Damage mechanism of composite laminates under multiple ice impacts at high velocity. *International Journal of Impact Engineering*, **168**, 104296, <https://doi.org/10.1016/j.ijimpeng.2022.104296>.

Appendix A: An erosion atlas for the contiguous United States of America

Reference: Pryor S.C., Coburn J.J. and Barthelmie R.J. (2025): Spatio-temporal Variability in Wind Turbine Blade Leading Edge Erosion. *Energies* **18**, 425 doi: 10.3390/en18020425

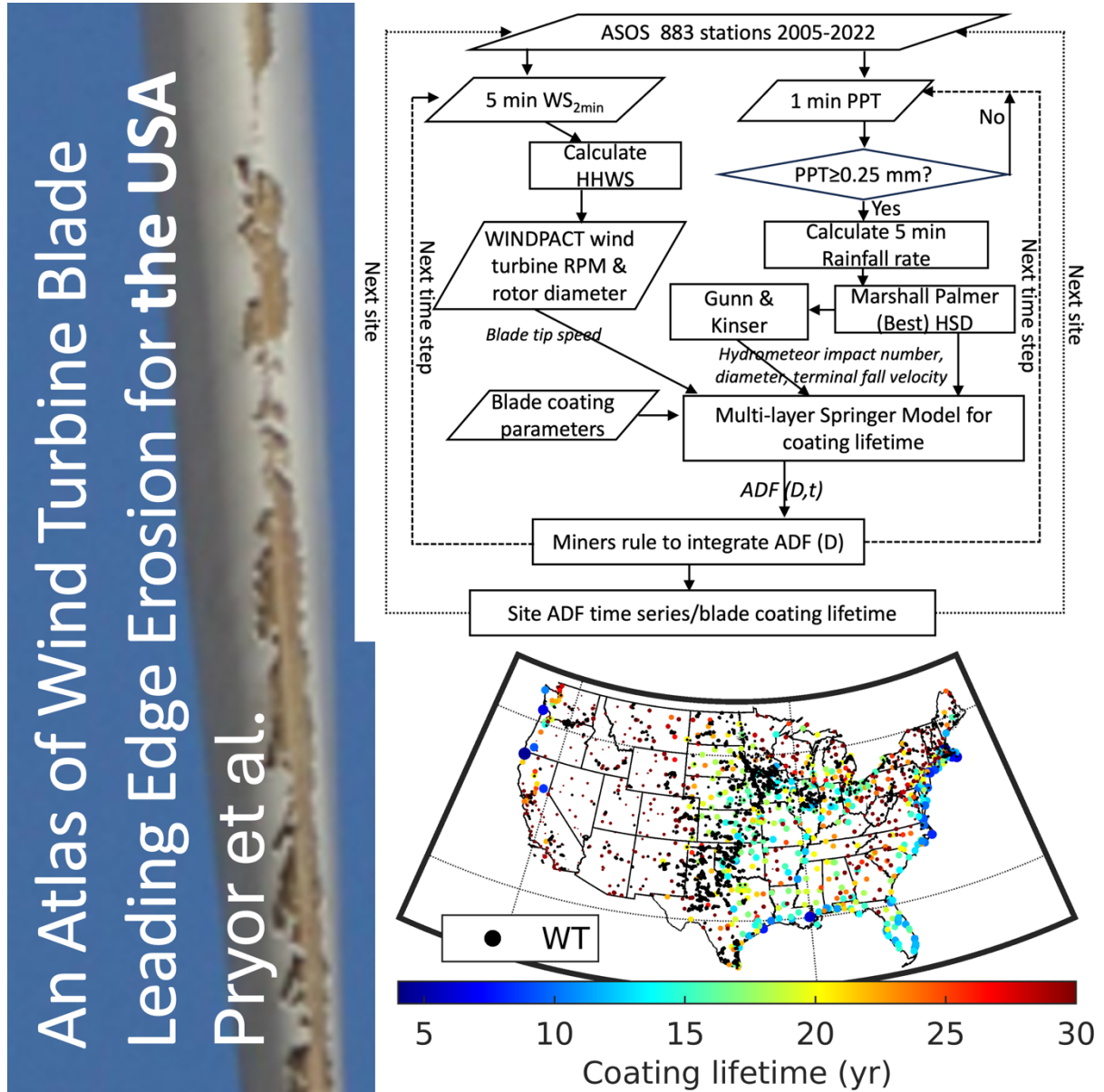





Figure 3 Summary of the methodology, and locations of currently operating wind turbines in CONUS and coating lifetime estimations.

Article

Spatiotemporal Variability in Wind Turbine Blade Leading Edge Erosion

Sara C. Pryor ^{1,*} , Jacob J. Coburn ¹  and Rebecca J. Barthelmie ² ¹ Department of Earth and Atmospheric Sciences, Cornell University, Ithaca, NY 14853, USA; jjc457@cornell.edu² Sibley School of Mechanical and Aerospace Engineering, Cornell University, Ithaca, NY 14853, USA; rb737@cornell.edu

* Correspondence: sp2279@cornell.edu; Tel.: +1-607-255-3376

Abstract: Wind turbine blade leading edge erosion (LEE) reduces energy production and increases wind energy operation and maintenance costs. Degradation of the blade coating and ultimately damage to the underlying blade structure are caused by collisions of falling hydrometeors with rotating blades. The selection of optimal methods to mitigate/reduce LEE are critically dependent on the rates of coating fatigue accumulation at a given location and the time variance in the accumulation of material stresses. However, no such assessment currently exists for the United States of America (USA). To address this research gap, blade coating lifetimes at 883 sites across the USA are generated based on high-frequency (5-min) estimates of material fatigue derived using a mechanistic model and robust meteorological measurements. Results indicate blade coating failure at some sites in as few as 4 years, and that the frequency and intensity of material stresses are both highly episodic and spatially varying. Time series analyses indicate that up to one-third of blade coating lifetime is exhausted in just 360 5-min periods in the Southern Great Plains (SGP). Conversely, sites in the Pacific Northwest (PNW) exhibit the same level of coating lifetime depletion in over three times as many time periods. Thus, it may be more cost-effective to use wind turbine deregulation (erosion-safe mode) for damage reduction and blade lifetime extension in the SGP, while the application of blade leading edge protective measures may be more appropriate in the PNW. Annual total precipitation and mean wind speed are shown to be poor predictors of blade coating lifetime, re-emphasizing the need for detailed modeling studies such as that presented herein.



Academic Editor: Davide Astolfi

Received: 20 December 2024

Revised: 12 January 2025

Accepted: 14 January 2025

Published: 19 January 2025

Citation: Pryor, S.C.; Coburn, J.J.; Barthelmie, R.J. Spatiotemporal Variability in Wind Turbine Blade Leading Edge Erosion. *Energies* **2025**, *18*, 425. <https://doi.org/10.3390/en18020425>

Copyright: © 2025 by the authors. Licensee MDPI, Basel, Switzerland. This article is an open access article distributed under the terms and conditions of the Creative Commons Attribution (CC BY) license (<https://creativecommons.org/licenses/by/4.0/>).

Keywords: blades; CONUS; hydroclimate; LCoE; LEE; operations and maintenance; Springer model; USA; wind energy

1. Introduction

1.1. Motivation: Wind Turbine Blade Leading Edge Erosion

Wind turbines are a low-cost, low-carbon electricity generation source and thus an effective means to reduce climate forcing [1,2]. Accordingly, the global wind energy installed capacity passed 1 TW in 2023 and is projected to surpass 2 TW before 2030 [3]. In the United States of America (USA), wind turbines contributed over 450 TWh of electricity to the grid (over 10% of national consumption) in 2023 [4] from an installed capacity of approximately 150 GW [3].

The efficiency of electricity generation, as measured using capacity factors (ratio of annual energy production (AEP) to maximum AEP of all wind turbines operated at their rated capacity all of the time), for wind turbines installed in the USA between 2009 and

2020 increased from 0.29 to 0.41 [5]. This is due in part to increasing wind turbine rated (or nameplate) capacity [6] and wind turbine dimensions, including rotor diameter, which increases the blade tip speed [7].

The levelized cost of energy (LCoE) from a generation source is given as follows:

$$\text{LCoE} = \frac{\sum_{n=1}^i (\text{CAPEX}_n + \text{O\&M}_n) / (1 + r)^n}{\sum_{n=1}^i \text{AEP}_n / (1 + r)^n} \quad (1)$$

where CAPEX_n = capital expenditures in year n , O\&M_n = operations and maintenance costs in year n , AEP_n = annual electricity production in year n , where $n = 1$ to i , where i is the lifetime, and r = discounting rate.

Inflation-adjusted LCoE in USD 2020/MWh from wind installations in the USA approximately halved between 2009 and 2020 [8], in part due to reductions in O&M costs [8]. Future O&M cost estimates are uncertain, but there is evidence that they are an increasing component of LCoE [9].

Wind turbine blades are multi-layered, comprising an outer coating layer that is designed to protect the underlying glass fiber (or carbon fiber)-reinforced polymer that is applied to a load-carrying shell [10]. Blade integrity is essential to efficient electrical power generation from wind turbines (AEP) and blades significantly contribute to both overall purchase price (>20% of CAPEX, [11]) and O&M costs [12,13]. During 2019, global O&M costs for onshore wind farms exceeded USD 15 billion with over half of expenditures being on unplanned repairs [14]. Past research has reported blade damage as the major cause of wind turbine failures [15]. A sample of 5800 wind turbine failure events during 1993 and 2006 found blade repairs typically took between 260 and 340 h [16]. One analysis found that “preventive maintenance could reduce the average lifetime maintenance cost 11.8 times comparing the corrective maintenance for wind turbine blades” [17].

An important cause of blade damage and degraded aerodynamic performance is leading edge erosion (LEE) [18]. LEE involves material loss of blade coatings, leading to exposure and loss of the glass fiber laminate. The resulting roughening of the blade [19] reduces lift and increases drag, leading to reduced power production (AEP) [20–24]. Accordingly, a range of techniques have been proposed to more efficiently detect blade damage to inform possible repair [25,26], and a number of research projects have been initiated to predict and reduce LEE [18]. The issuance of testing standards for erosion resistance of leading edge protective (LEP) products by Det Norske Veritas (DNV) in 2020 further emphasizes the importance of LEE to the wind energy industry [27].

Recent research on indicative costs for repair of LEE as a function of damage severity report ranges (for 3 blades) from GBP 7000 for minor damage (categories 1–2, discoloration of coating to removal of up to 10 cm² of coating) to GBP 42,000 for major damage (category 4, coating removed and partial removal of first layer of laminate, resulting in AEP losses of 3%) to GBP 3,750,000 (category 5, holes in laminate, loss of AEP ≥ 5%) [28] (estimated AEP loss as a function of damage severity from [19]). While relatively few wind farm owner-operators have released information regarding the extent or timing of LEE emergence, according to one report when EDP Renewables inspected 201 rotor blades on a wind farm after 14 years of operation, 174 blades (87%) had visible signs of erosion, and 100 blades (50%) showed severe LEE [29]. Further, an analysis of wind turbine blades from India found evidence of LEE in as little as two years of operation [30]. Slowing/mitigating coating failure and LEE and thus extending blade lifetimes has the potential to contribute further reductions in LCoE from wind turbines via both increased AEP and reduction of O&M costs and may aid in partially alleviating cost/environmental issues linked to recycling/disposal of blades [31].

LEE is primarily the result of material stresses induced when hydrometeors (i.e., rain droplets, hail stones) impact on rapidly rotating blades [32–36]. Experimental data and detailed modeling using finite element methods indicate that the impact force and von Mises stresses in coatings for individual hydrometeor impacts scale with impact velocity and hydrometeor mass and hence diameter [37–39]. Hence, impacts from larger hydrometeors lead to coating failure with fewer impacts per unit area because they have higher kinetic energy of impact and induce both larger stress values at the impact site and stress waves that travel further through the material [39]. Therefore, the cumulative material stresses in blade coatings from hydrometeor impacts are amplified under the following conditions:

- Under high wind speeds when closing velocities (v_c) between the hydrometeors and the rotating blade are maximized. v_c is typically dominated by the blade tip speed (Figure 1a) which exceeds the terminal fall velocity (v_t) of hydrometeors (Figure 1b) frequently by an order of magnitude.
- During periods of intense precipitation when there are many, and larger, hydrometeors [38] (Figure 1c) and/or during periods of hail.

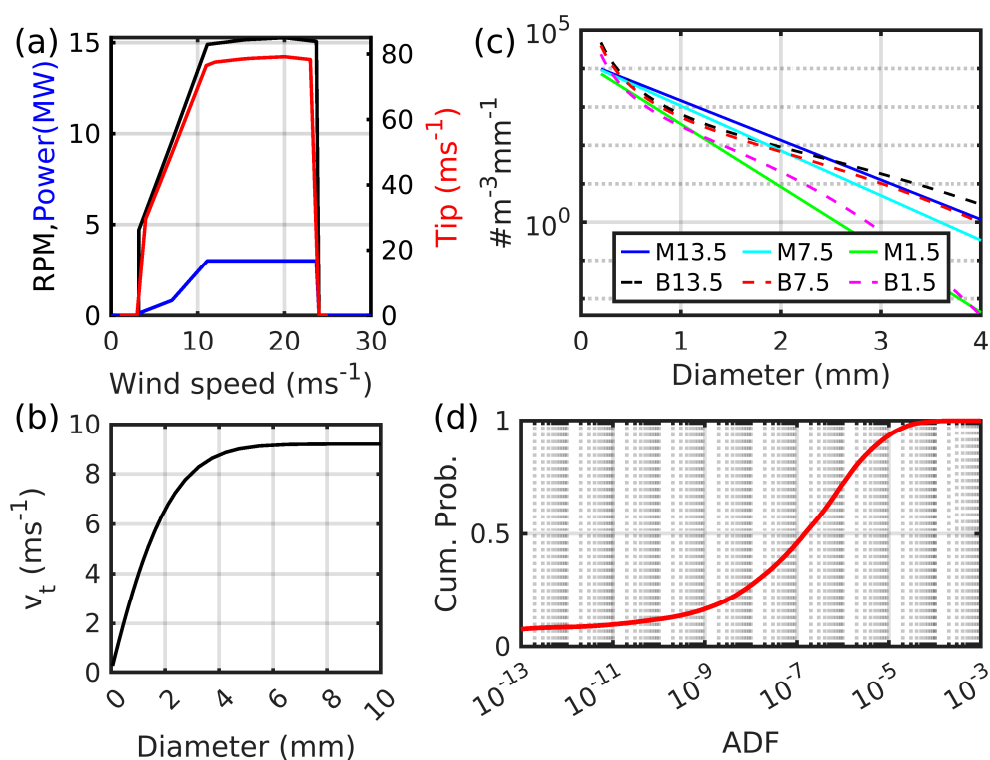


Figure 1. Overview of parameters that dictate wind turbine blade leading edge erosion. (a) Rotor rotational (RPM, black) and tip (Tip, red) speed and electrical power generation (Power, in MW, blue) as a function of the hub-height wind speed for the 3 MW WINDPACT reference wind turbine [40]. (b) Terminal fall velocity (v_t) as a function of hydrometeor diameter [41]. (c) Number density of rain droplets ($\# \text{m}^{-3}$ per mm of diameter space) computed using the Marshall–Palmer distribution approximation (prefix M) [42] and the approximation of Best [43] (prefix B) for three different rainfall rates (in mmhr^{-1}). (d) Cumulative density function (CDF) of 1-min blade coating accumulated distance to failure (ADF) values computed using the Springer model [44,45] and 4 years of hydrometeor size distribution and wind speed measurements from the US Department of Energy’s Atmospheric Radiation Measurement (ARM) experimental station in the Southern Great Plains (location shown in Figure 2a by the magenta dot, see details in [46]).

Most wind turbines in the contiguous USA (CONUS) are deployed in locations with good wind resources, but also where hydroclimatic conditions associated with highest

material stresses and hence LEE potential are frequent (heavy precipitation and hail during periods with high wind speeds; thus, turbines are operating at maximum rotational speed) [35] (Figure 2a–c). Further, wind turbines being deployed offshore are physically larger and have both longer blades and higher tip speeds than those deployed onshore [3]. This leads to higher closing velocities with falling hydrometeors and thus potentially more rapid erosion in offshore locations that also have higher O&M costs [47] and are also experiencing pricing challenges linked to risk and cost of capital [48].

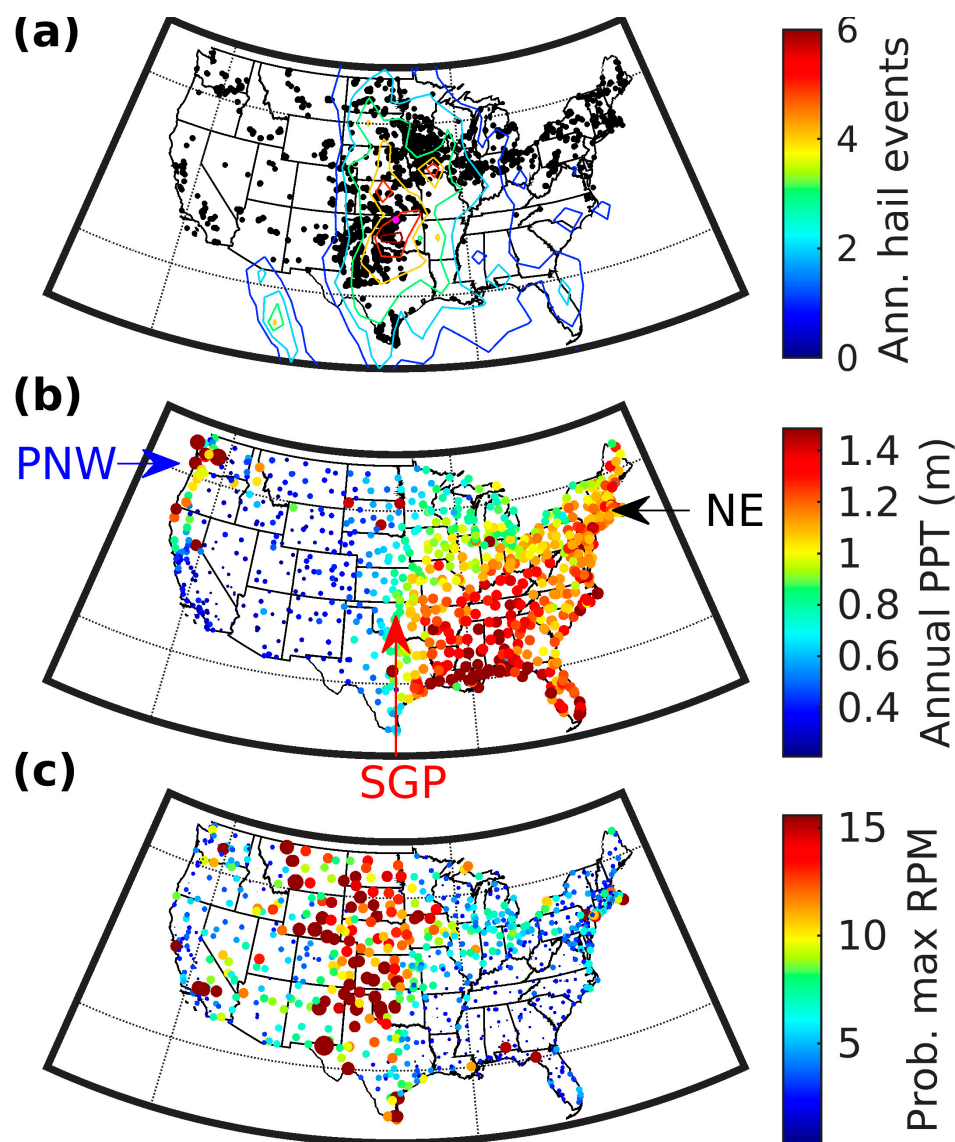


Figure 2. Overview of datasets. (a) Wind turbine locations in the CONUS at the end of 2023 based on data from the USGS Wind Turbine Database [49,50] (black dots). The magenta dot shows the location for which blade coating ADF estimates are shown in Figure 1d. Contours show estimated annual hail frequency from the NASA Passive Microwave Hail Climatology Data Products V1 dataset [51]. (b) Annual total precipitation at the Automated Surface Observing Station (ASOS) sites computed using 1-min observations from 2005 to 2022. (c) Probability that the wind speed at the hub height (90-m) of the 3 MW WINDPACT reference wind turbine is in the range with maximum rotor rotational speed (RPM, Figure 1a) based on ASOS observations to 10-m height and application of the power law (see Equation (2)). The arrows and text (PNW, SGP, and NE) in frame (b) show the locations used to illustrate the time series of ADF. Color bar limits in (b,c) are set to 5th to 95th percentile values to aid legibility of spatial gradients.

Options for reducing wind turbine blade LEE include the following:

- (i) Redesign of blades, use of more energy absorbing materials in coatings or reduction of manufacturing defects [52–54]. These may increase manufacturing, and hence CAPEX costs, and they can only be applied to new wind turbines.
- (ii) Use of leading edge protection (LEP) products [55,56]. The application of LEP as part of the blade manufacture or after wind turbine deployment will increase CAPEX or O&M costs, respectively. Use of LEP may also negatively impact blade aerodynamics, resulting in reduced AEP [21,57,58].
- (iii) Dynamical operation of wind turbines to reduce rotor speed during periods associated with high material stresses (i.e., intense precipitation at high operating wind speeds) [32]. This erosion-safe mode operation necessarily reduces AEP due to the loss of electricity production during curtailment/deregulation to slow rotor speeds, but may decrease O&M costs by increasing blade coating lifetimes, leading to a net benefit in terms of LCoE [46].

Cost–benefit analyses designed to select between options (ii) and (iii) for a given environment are critically reliant on modeling using the joint probability distributions of wind speeds and hydroclimate properties that dictate material stresses in blade coating and LEE.

The ASOS observations used in the current analysis illustrate the presence of marked geospatial variability in annual total precipitation (Figure 2b) and the frequency with which wind turbines are likely to have their blades rotating at the maximum speed (Figure 2c). There is, therefore, an expectation that wind turbine blade coating lifetimes will equally exhibit high spatial variability across North America. No comprehensive geospatial description of blade coating lifetimes is currently available for the CONUS, but past research using wind speeds and precipitation estimated from six National Weather Service RADARs demonstrated very high spatial variability in precipitation-induced blade coating damage potential and indicated the importance of low-probability, high-impact events to cumulative annual total kinetic energy transfer [36]. Analyses for a site in the Southern Great Plains (SGP) region of the USA also showed that the probability distribution of high-frequency accumulated distance to failure (ADF) of blade coatings due to hydrometeor-induced stresses is extremely heavy tailed. That is, when ADF estimates are derived using the Springer model applied to 1-min resolution hydrometeor size distribution and hub-height wind speed measurements, relatively few 1-min periods dominate the accumulation of material stress (Figure 1d) and hence the duration of time required for onset of erosion (when $ADF = 1$) [46].

In analyses of data from the SGP where total ADF is dominated by a few time periods, modeling using rotor-speed curtailment during the most erosive 0.1–0.2% of 10-min periods (i.e., enactment of option (iii) erosion-safe mode) was found to substantially increase blade coating lifetimes and thus lead to a minimized LCoE despite the associated loss of power production and hence revenue [46]. Conversely, in a situation where ADF increments occur in more numerous and more evenly weighted periods, option (ii) may be preferable in terms of net impact on LCoE. Selecting between options (ii) and (iii) will necessarily depend on the cost of blade repair, purchase of LEP products, and their deployment costs [28], as well as quantification of the amount of time when erosion-safe mode operation is required and, thus, how much AEP is sacrificed. Hence, market conditions, such as the purchase price of electricity, which exhibits marked variations in time and space, must also be considered [59,60]. For this reason, it is useful, as herein, to quantify not only wind turbine blade coating lifetimes but also the frequency of periods that cause large material stress (ADF increments) and the seasonality of these highly erosive periods. Such information can

facilitate economic modeling by wind farm owner operators to select the most appropriate LEE mitigation approach in each location.

1.2. Objectives

Our primary objective is to develop and present the first geospatial description of wind turbine blade coating lifetime and hence LEE potential for the continental USA (CONUS) that can be used to aid in decision making for wind farm owner-operators with respect to adoption/selection of LEE mitigation measures. Importantly, the modeling presented herein not only quantifies the duration of time prior to coating failure and erosion onset but is also used to quantify the degree to which coating ADF at each location exhibits evidence of being dominated by relatively few extreme events and their seasonality. This information is essential for costing of each LEE mitigation option at a given location.

2. Materials and Methods

2.1. Meteorological Observations

Precipitation intensity is zero-bounded, and the probability distribution is both heavy tailed and dependent on spatial and temporal resolution of the data and hence the degree of averaging [61–63]. As described above, high ADF values occur during periods of very intense precipitation and high wind speeds when many, large hydrometeors (Figure 1c) collide with a rapidly rotating blade at high closing velocities (Figure 1a,b). Hence, there is evidence that the probability distribution of high-frequency ADF increments for blade coatings may also be heavy tailed (Figure 1d). Thus, it is essential to use high-frequency meteorological data to generate wind turbine blade coating lifetime estimates and thus the expected duration of time prior to LEE.

The full research methodology applied in this work is detailed below with a schematic workflow also given in Figure 3. The first step is to describe the prevailing meteorological conditions at each location. To do so, we use records from 883 National Weather Service (NWS) Automated Surface Observing System (ASOS) network stations, covering the period from 2005 to 2022. These records include 1-min accumulated precipitation plus 2-min sustained wind speed within a 5-min period. The ASOS network is subject to stringent site selection [64], instrument maintenance [65], and data quality assurance protocols [66]. Sustained wind speed measurements at 10-m height are obtained using a heated 2D sonic anemometer [67]. They are reported herein in ms^{-1} , but are recorded in whole knots with values below 3 knots reported as 0 [68]. Accumulated precipitation measurements are taken using a heated and wind-shielded tipping bucket rain gauge [69,70]. The minimum 1-min precipitation depth is 0.01 inch (0.254 mm) and is equal to one tip of the pivoted bucket within the rain gauge. One-minute accumulated precipitation is aggregated to 5-min periods for which wind speeds are reported and converted to a rainfall rate in mmhr^{-1} . Blade coating lifetime statistics presented herein are corrected for missing data periods to generate an effective 18-year blade coating ADF. Three of the 883 ASOS stations have <50% of possible observations available and are excluded from further analyses.

The WINDPACT reference wind turbine [40] used in this analysis to derive 5-min time series of blade rotational speed as a function of prevailing wind speed (Figure 1a). This wind turbine has a rated capacity of 3 MW and hub height of 90-m and thus is a reasonable representation of the average of the current US wind turbine fleet [4]. ASOS wind speeds as measured at 10-m (WS_{10}) are scaled to the hub height of 90-m (WS_{90} , referred to here as WSHH) using the power law and a coefficient of $1/7$ [71]:

$$WS_{90} = WS_{10} \times \left(\frac{90}{10}\right)^{1/7} \quad (2)$$

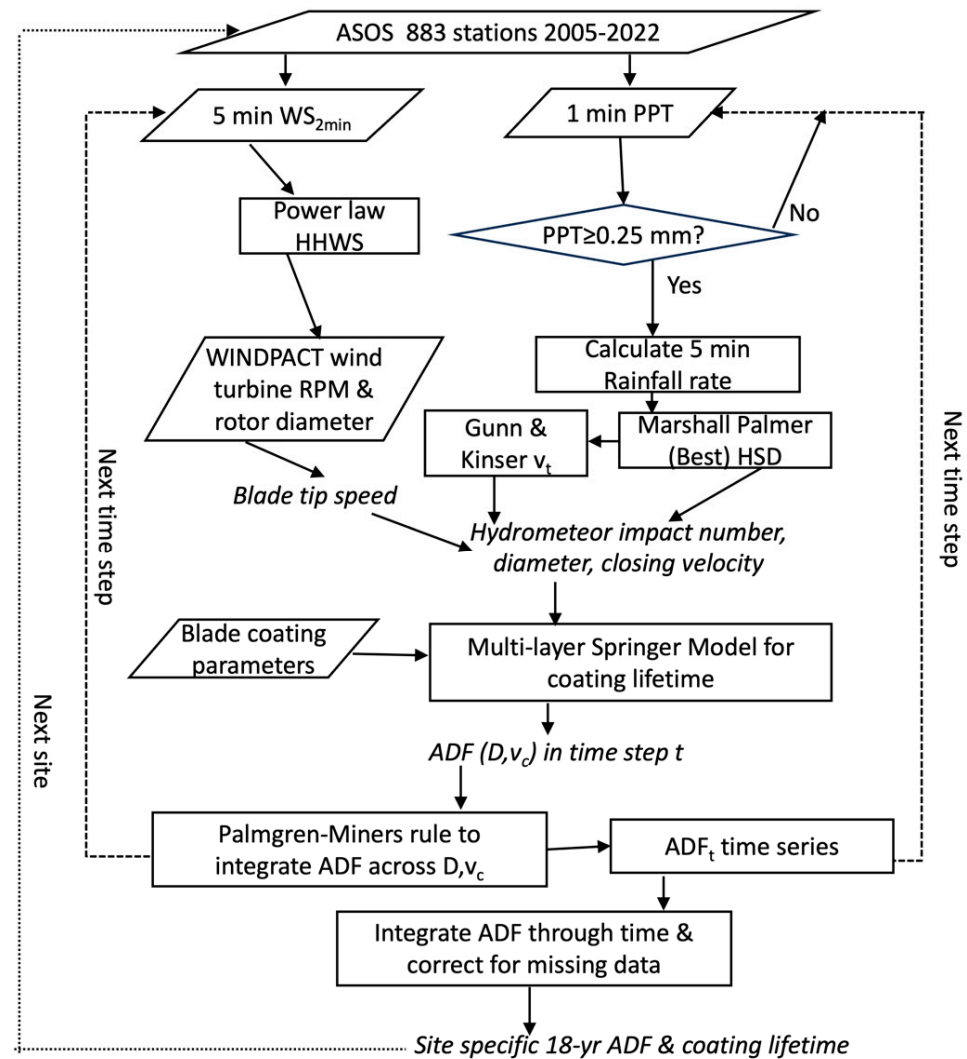


Figure 3. Flowchart presenting the workflow used to create a time series of 5-min blade coating accumulated distance to failure increments (ADF_t), 18-year ADF and blade coating lifetimes for each site.

Thus, the scaling factor applied to the ASOS 5-min interval wind speed measurements for use in determining the blade rotational speed and tip speed is 1.38.

To illustrate variations in 5-min coating ADF increments as derived using the ASOS measurements and the Springer model in different climates and regions of the CONUS, we present data from indicative stations in the Pacific Northwest (PNW) from KAST in Astoria, Oregon; Southern Great Plains (SGP) from KOKC in Oklahoma City, Oklahoma; and the Northeast (NE) from KACK in Nantucket, Massachusetts. These locations are close to major wind turbine deployments (Figure 2a). The PNW experiences high annual total precipitation (Figure 2b). The SGP has the greatest concentration of wind turbines and an extreme hydroclimate with a high frequency of deep convection and intense precipitation [72,73] (Figure 2a,b). The NE site is selected to be close to the US eastern coastline and hence adjacent to areas where major offshore wind energy installations are currently underway [74].

2.2. Mapping Atmospheric Drivers to Damage

Multiple engineering models have been developed to simulate the material stresses induced by hydrometeor collisions with the wind turbine blade that cause coating degradation and lead to blade LEE [38,75,76]. Herein, we employ a multi-layer version of the

Springer model [44,45,77–79] that uses the material properties of the blade and coating to compute the number of impacts required for failure per unit area (N_i , m^{-2}) for a given hydrometeor diameter (D , m), impact velocity (v_c , ms^{-1}), and impact angle (θ). Using the integration of hydrometeor diameter, closing velocity, and then time, the model can be used to derive an accumulated distance to failure of the coating and hence onset of blade erosion. The Springer model has been widely described and validated relative to rain erosion tests [78] and is also employed within the recommended practice (RP) for evaluation of erosion and delamination for leading edge protection systems of rotor blades issued by DNV [27].

The fundamental equations of the Springer model are presented below. A range of coefficient values have been postulated to represent wind turbine blade materials [79]. Hence, the values of the model coefficients used in the current research are given below along with the reference from which the values are drawn.

$$N_i = \frac{4\pi}{D^2} a_1 \left(\frac{S_{ec}}{\sigma_0} \right)^{a_2} \quad (3)$$

where S_{ec} = erosion strength of the coating. In addition, a_1 and a_2 are constants that in the current implementation of the model have values of 7×10^6 and 5.7, respectively [79]. Here, σ_0 = average stress of the coating surface, and scales with the thickness of the coating, the coating and substrate material properties, and the hydrometeor diameter and is expressed as follows:

$$\sigma_0 = v_c \frac{Z_L \cos(\theta) (\psi_{sc} + 1)}{\left(\frac{Z_L}{Z_c} + 1 \right) (1 - \psi_{sc} \psi_{Lc})} \left(1 - \frac{(1 - e^\gamma) (\psi_{Lc} + 1) \psi_{sc}}{\gamma (\psi_{sc} + 1)} \right) \quad (4)$$

where v_c = impact velocity (set as the closing velocity between the hydrometeor and the blade); θ = impact angle between the hydrometeor and the blade (assumed here to be 0, i.e., there is no deflection of the hydrometeor and the impact is normal to the leading edge [79]); Z_x = impedance of each material; and $\rho_x C_x$, where ρ_x = material density. In the following, subscripts (x) are used to refer to L = liquid, c = coating, and s = substrate. Here, ρ = material density: $\rho_c = 1690 \text{ kgm}^{-3}$ [78], $\rho_L = 997 \text{ kgm}^{-3}$ [79] and $\rho_s = 1930 \text{ kgm}^{-3}$ [78]. C = elastic wave speed: $C_L = 1481 \text{ ms}^{-1}$ [79], $C_c = 1730 \text{ ms}^{-1}$ [78,79] and $C_s = 2390 \text{ ms}^{-1}$ [78]. ψ_{xx} = relative acoustic impedance, where sc = substrate coating and Lc = liquid coating.

$$\psi_{sc} = \frac{Z_s - Z_c}{Z_s + Z_c} \quad (5)$$

$$\psi_{Lc} = \frac{Z_L - Z_c}{Z_L + Z_c} \quad (6)$$

Here, γ = coating thickness parameter (maximum number of reflections during the impact time within the coating thickness) and is expressed as follows:

$$\gamma = \frac{2C_c Z_c (Z_L + Z_s) D}{C_L (Z_c + Z_L) (Z_c + Z_s) h} \quad (7)$$

where h = coating thickness. A range of blade coating thicknesses are reported in the literature. For example, values of 100 to 3000×10^{-6} m are given in [75]. Increasing the coating thickness reduces the number of stress reflections at the coating/substrate boundary. Thus, for given substrate impedance, the ratio $\frac{S_{ec}}{\sigma_0}$ and hence the number of impacts to

failure from Equation (3) are minimized for high D to h ratios [75]. In the current research, h is set to 750×10^{-6} m [79].

$$S_{ec} = \frac{4(b_c - 1)\sigma_{Uc}}{(1 - 2\nu_c)\left(1 - \left(\frac{\sigma_{Ic}}{\sigma_{Uc}}\right)^{b_c - 1}\right)(2k|\psi_{sc}| + 1)} \quad (8)$$

where σ_{Uc} = coating ultimate tensile strength (1.30×10^7 Pa [78]), σ_{Ic} = coating endurance limit (6.30×10^6 Pa [78]), and b_c = coating Springer fatigue knee, which is computed from the material fatigue knee (b_{2c} , 16.52 [78]) as follows:

$$b_c = \frac{b_{2c}}{\log_{10}\left(\frac{\sigma_{Uc}}{\sigma_{Ic}}\right)} \quad (9)$$

where ν_c = coating Poisson ratio (0.295 [78]). Here, k is given as follows:

$$k = \frac{1 - e^{-\gamma}}{1 - \psi_{sc}\psi_{Lc}} \quad (10)$$

Palmgren–Miner’s rule is used to integrate across all hydrometeor D and closing velocities to quantify the accumulated distance to failure (ADF_t) of the blade coating in each 5-min period [78,79]:

$$ADF_t = \sum_{d=1}^{d=kk} \sum_{v=1}^{v=mm} \frac{N(d,v)}{N_i(d,v)} \quad (11)$$

where ADF_t is the accumulated distance to failure of the blade coating in time interval t; d is the hydrometeor diameter class (d = 1 to kk, where kk is the largest hydrometeor diameter class considered); v is the closing velocity class (v = 1 to mm, where mm is the largest class of closing velocity considered); $N(d,v)$ is the number of impacts in each diameter and velocity class; and $N_i(d,v)$ is the number of impacts in that diameter and velocity class to failure (see Equation (3)).

Integration of ADF_t through time is used to define the duration of time required for the accumulated number of impacts in each diameter and closing velocity class required to reach $ADF = 1$. When $ADF = 1$, this indicates the end of the incubation period where stress is accumulated by the surface, but the aerodynamic performance is virtually unaffected. $ADF = 1$ indicates the onset of erosion, mass loss from the blade, and degradation of blade aerodynamic performance. The coating lifetime in fraction of years is thus the duration of time elapsed for ADF to reach a value of 1.

The Springer model also requires information regarding the hydrometeor size distribution (HSD, hydrometeor counts in diameter classes). Herein, we employ the Marshall–Palmer approximation [42] to generate these HSDs:

$$N = \frac{N_0}{\Lambda} e^{-\Lambda R} \quad (12)$$

where N = number of droplets above radius, R (m), per cubic meter of air ($\#m^{-3}$); $\Lambda = 8200 \times RR^{-0.21}$ (m^{-1}); $N_0 = 1.6 \times 10^7 m^{-4}$; and $RR =$ rainfall rate ($mmhr^{-1}$) (Figure 1c). For comparative purposes, we also present example ADF increments based on analyses in which the HSD is computed using the approximation of Best [43]:

$$N = \frac{W}{V} \left(\frac{k_i \times D^{k_i-1}}{a^{k_i}} \right) e^{-[D/a]^{k_i}} \quad (13)$$

where N = number of droplets above diameter, D (in mm), per cubic meter of air ($\#m^{-3}$); V = droplet spherical volume (mm^3); W = total water volume ($67 \times RR^{0.846}$) (mm^3m^{-3}); $k_i = 2.25$; and $a = 1.3 \times RR^{0.232}$.

The modeling additionally requires information regarding hydrometeor fall velocity to estimate the closing velocity with the rotating blade. Herein, we use the terminal fall velocity (v_t) as a function of hydrometeor diameter from Gunn and Kinzer [41] (Figure 1b). The closing velocity (v_c) in each time step (t) and for each diameter (D) is a function of the terminal fall velocity (v_t) for that of a hydrometeor of a given diameter, horizontal wind speed at hub height (WSHH), linear speed of the blade tip (v_r), and blade position (ϕ):

$$v_c(D, t, \phi) = \left[WSHH^2 + (v_r + v_t(D) \times \cos\phi)^2 \right]^{1/2} \quad (14)$$

Thus, if $WSHH = 16 \text{ ms}^{-1}$, the blade tip speed is 78.7 ms^{-1} , and a 2 mm diameter hydrometeor falling at a v_t of 6.55 ms^{-1} will have a closing velocity with the blade that varies between 73.9 and 86.7 ms^{-1} depending on the blade position.

The total number of impacts of hydrometeors of a given diameter (D) on the blade leading edge during time interval t ($I(D, t)$), also known as the impact rate, is a function of the hydrometeor number density ($N(D)$) as described using Equations (12) or (13) and their closing velocity from Equation (14):

$$I(D, t) = N(D) \times v_c(D, t, \phi) \quad (15)$$

Five-minute rainfall rates (in $mmhr^{-1}$) and WSHH from ASOS observations are not continuous but rather take discrete values. Hence, a matrix of ADF values as a function of 41 WSHH values (0 to 40 ms^{-1}) and 51 RR values (0 to 150 mmhr^{-1}) was computed. This matrix comprises a look-up table (LUT) that is applied to time series from each ASOS station to determine the ADF increment (summed across all D) for every 5-min record of wind speed and rainfall rate (ADF_t). Summing the time and correcting for missing data periods, an effective 18-year blade coating ADF is computed for each ASOS location.

Two statistical metrics are presented to describe the concentration of coating ADF increments in time: (a) sum of the top n values from each time series of 5-min ADF_t , where n varies from 1 to 1000, and (b) probability that consecutive periods will exceed a specified ADF threshold. The frequency of occurrence of high ADF_t is also presented by computing the number of occurrences of $ADF_t > 1 \times 10^{-4}$ in each calendar month divided by the total number of observations in that month.

The heavy-tailed nature of the probability distributions of ADF_t has the implication that relatively long records of meteorological drivers are required to generate robust 18-year ADF and hence blade lifetime estimates at each site. To examine the importance of data record duration and the precise years present in the record, a resampling analysis using complete years is performed. In this analysis, 18-year ADF is computed using record lengths of 1 to 17 years with sampling of individual calendar years without replacement.

Confidential communication with a major wind farm owner-operator indicated that they purchase estimates of total annual precipitation and mean wind speed to provide preliminary information regarding the duration of time to coating failure at prospective development sites. Hence, a final analysis is performed to evaluate the degree to which the spatial variability in 18-year ADF can be explained by these variables. This analysis leverages linear regression with parameter fitting using maximum likelihood estimation.

3. Results

3.1. Simulated Blade Coating Lifetime as a Function of Prevailing Meteorology

Figure 4a presents a heatmap of 5-min accumulated distance to failure (ADF_t) for blade coatings, integrated across all hydrometeor diameters for example combinations WSHH and RR where the number concentration of hydrometeors of each diameter is computed using the Marshall–Palmer approximation. While the absolute values of 5-min ADF increments are naturally dictated by the coefficients used in the Springer model, this heatmap illustrates several key points. First, based on the multi-layer Springer model, hydrometeors associated with RR of 15 mmhr^{-1} , across all wind speeds and hence rotor speeds, are >6 times as efficient at causing material stresses, and contributing to ADF increments, than those associated with a RR of 1.5 mmhr^{-1} . Second, because the closing velocity between the hydrometeors and the blade is highly dependent on the rotational rate of the wind turbine blades, periods when the WSHH is at, or close to, the inflow wind speed with maximum RPM are particularly important to the ADF . For a RR of 4.5 mmhr^{-1} , there is 50-fold higher 5-min ADF increment when wind speeds are 16 ms^{-1} versus 3.25 ms^{-1} . Third, accurate specification of the frequency of conditions in differing rain rate and wind speed classes is critical to determining ADF of wind turbine blade coatings and hence the likelihood of LEE in a given time interval. Finally, the approximation applied to compute the HSD plays a role in the absolute values of blade coating ADF for a given rain rate and wind speed (cf. Figure 4a,b). ADF is larger when the HSD is computed using the formulation of Best (Equation (13)) versus that of Marshall–Palmer (Equation (12)). Thus, coating lifetimes would be shorter if the Best HSD were applied. For the example WSHH and RR illustrated in Figure 4, the ratio of ADF increments from calculations using Best versus Marshall–Palmer range from 2.52 for low rainfall rates (1.5 mmhr^{-1}) to 1.43 for high rainfall rates (15 mmhr^{-1}).

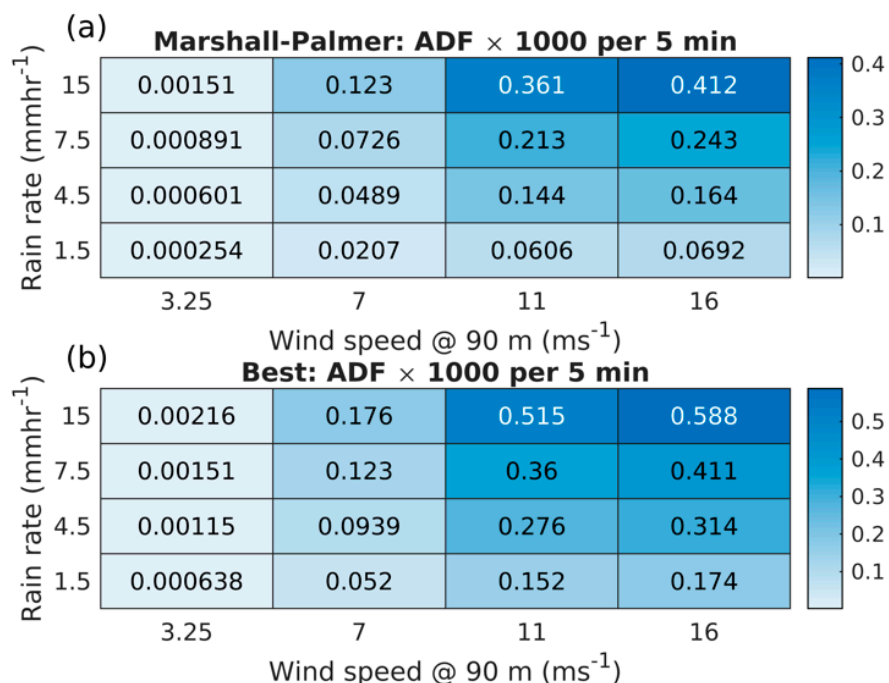


Figure 4. A heatmap of blade coating ADF_t ($\times 10^3$ to aid visibility) for 5-min periods with example wind speeds and rainfall rates. ADF_t computed using (a) HSD from Marshall–Palmer and (b) HSD from Best. ADF_t is computed using the Springer model, the closing velocity derived using the WINDPACT 3 MW reference turbine and hydrometeor, and v_t from Gunn and Kinzer [41].

3.2. Geospatial Variability of Blade Coating Lifetime

In accord with a priori expectations and limited past research [36], the blade coating lifetime estimates across the CONUS exhibit marked geospatial variability. Here, 18-year ADF estimates range from <0.1 at the ASOS sites with the least erosive climate to a maximum of 4 (Figure 5a). A value of 4 indicates that a blade coating with the material properties employed in the Springer model is projected to fail 4 times during an 18-year period. Alternatively stated, the blade coating is expected to fail, on average, in just over 4 years. Analyses for one-quarter of the ASOS stations indicate an 18-year $ADF > 1$, and two-thirds of sites have a $ADF > 0.5$. Stations with 18-year $ADF > 1$ that are close to current wind turbine installations (Figure 2a) are clustered along the US west coast, in the Central Plains, and along the US east coast (Figure 5a). Several sites exhibit blade coating lifetimes of <12 years (Figure 5b). The site with the highest 18-year ADF (4) is KCEC in Crescent City, California. This coastal station experiences high annual total precipitation (1539 mm) and a relatively high frequency of precipitation during periods when the wind speed is such that the reference wind turbine would be operating at high RPM.

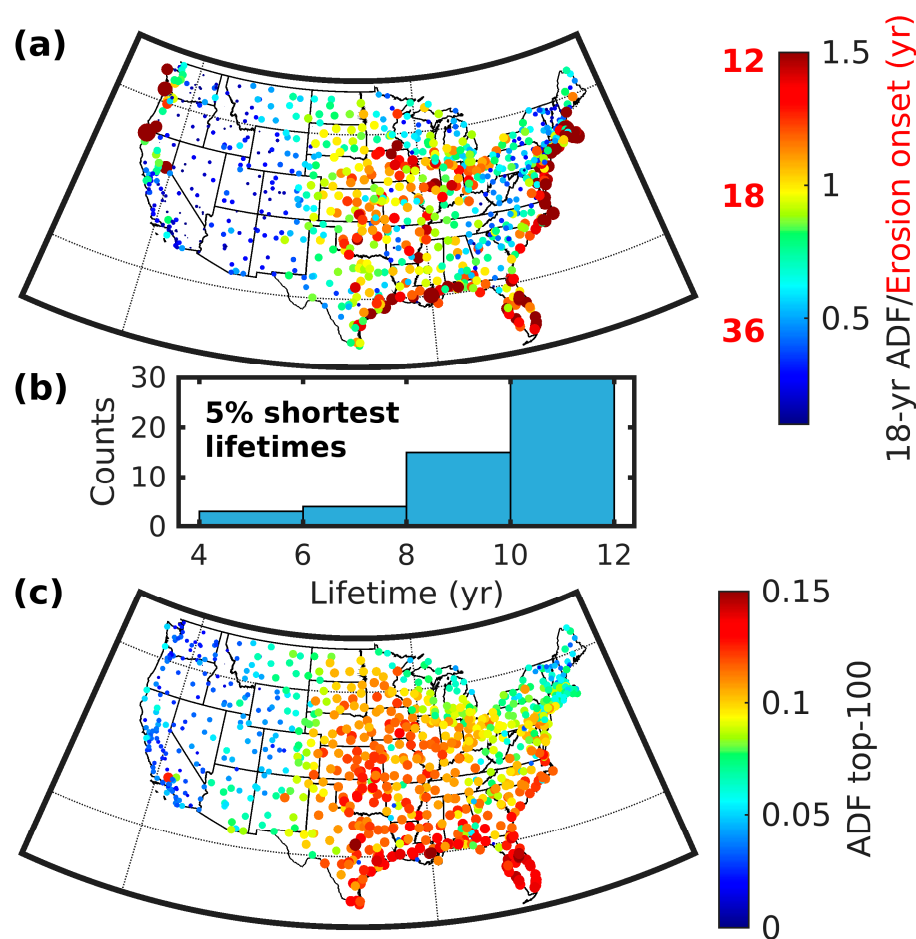


Figure 5. Blade coating lifetimes. (a) Eighteen-year accumulated distance to failure (ADF) and coating lifetime (erosion onset time in years) at each of the ASOS sites. A value of 1 indicates that the coating lifetime has been exhausted in 18 years, and blade damage is predicted to have commenced. (b) Histogram of the coating lifetimes for the top 5% of ASOS sites with the highest 18-year ADF (i.e., 18-year $ADF > 1.5$). (c) The ADF from the top 100 most erosive 5-min periods during the measurement record. Color bar limits in panels (a) are set to 5th to 95th percentile values to aid legibility of spatial gradients.

Data regarding the need for blade repair or LEP application are generally kept confidential by wind farm owner-operators. Thus, it is difficult to evaluate the coating lifetime

predictions presented in Figure 5a. An earlier analysis using independently measured HSD and fall velocities from a disdrometer and wind speeds from a lidar at the US Department of Energy Atmospheric Radiation Measurement (DoE ARM, see location in Figure 2a) site in Lamont, Oklahoma predicted the 3 MW reference turbine would experience coating failure in slightly over 16 years (see cumulative density function of 1-min ADF increments from that analysis in Figure 1d) [46]. Analyses presented herein for an ASOS site 32 km from the ARM location are consistent with that earlier work and indicate an ADF of 1 over the 18-year period (i.e., a coating lifetime of ≤ 18 years).

3.3. Temporal Variability in Blade Coating Lifetime Reduction

The probability distributions of 5-min ADF increments varies markedly across the USA. Accordingly, the contribution of the top 100, 5-min periods in terms of incremental contributions to ADF also exhibits marked spatial variability (Figure 5c). Over much of the western half of the CONUS, the top 100 most erosive 5-min periods contribute less than 5% of the total 18-year ADF, and $<5\%$ of a blade coating lifetime. In other locations, for example much of the SGP, values exceed 0.1, indicating that 10% of the coating lifetime may be exhausted during as few as 100 5-min periods. The top 100 5-min ADF values along the Gulf coast of the CONUS (i.e., the southeastern USA) are also very high likely due, in part, to torrential rain and high wind speeds associated with land-falling tropical cyclones [80,81].

Analyses of modeled time series from three example ASOS stations with 18-year ADF > 1.5 that are located close to major wind turbine installations indicate marked variations in the degree to which the ADF time series is heavy tailed (Figure 6a).

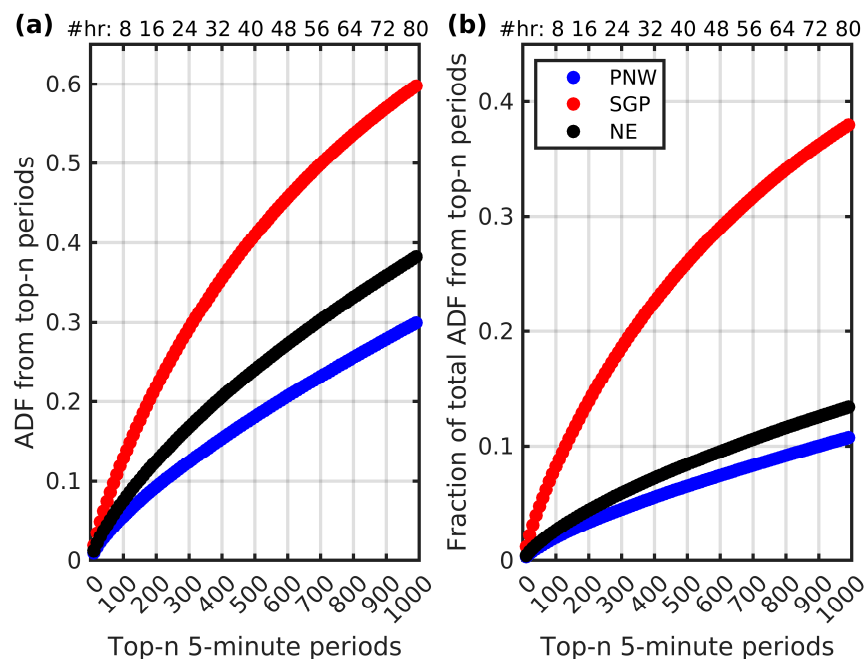


Figure 6. Concentration of blade coating accumulated distance to failure (ADF) in time. (a) ADF increment during the top-n most erosive 5-min periods (top axis = equivalent number of hours) at three example sites where 18-year ADF exceeded 1.5. (b) Fraction of total 18-year ADF contributed by the top-n most erosive 5-min periods (top axis = equivalent number of hours) at three example sites where 18-year ADF exceeded 1.5. Pacific Northwest (PNW) reports data from KAST in Astoria, Oregon (18-year ADF of 2.8). Southern Great Plains (SGP) reports data from KOKC in Oklahoma City, Oklahoma (18-year ADF of 1.6). Northeastern US (NE) reports data from KACK in Nantucket, Massachusetts (18-year ADF of 2.9) (see site locations in Figure 2).

The SGP site achieves an ADF of 0.33 (i.e., one-third of blade coating lifetime expended) in just 360 5-min periods (or 30 h) (Figure 6a). For the PNW site, 1130 5-min periods are required to achieve an ADF of 0.33. For the NE station, 790 5-min periods are required. Thus, approximately three times as many 5-min periods are required in the PNW to achieve the same accumulated level of material stress as the top 360 periods in the SGP. The dominance of a few extremely erosive periods in determining overall total 18-year ADF across these sites is even more marked (Figure 6b). Over one-third of the total 18-year ADF at the SGP site is associated with ADF increments in just 1000 5-min periods or just over 80 h (Figure 6b). This implies that there may be the greatest value in the use of erosion-safe mode in the SGP, given that curtailment of electricity production will be required during only a small number of hours each year. Conversely, for the PNW site, only just over 10% of the 18-year ADF is accumulated in the top 1000 most erosive 5-min periods.

The likelihood of highly erosive periods (5-min ADF increments of $> 1 \times 10^{-4}$) in SGP is maximized during April–June (Figure 7a) likely due to the prevalence of deep convection during these months and the associated occurrence of high rainfall rates [73]. Thus, the adoption of erosion-safe mode to extend blade lifetimes would likely be most frequent during the spring and early summer, before the peak electricity demand, which occurs during July and August in Oklahoma (data from the US Energy Information Administration (EIA) <https://www.eia.gov/>, accessed on 2 November 2024). Highly erosive periods in the PNW are confined to winter during the season of strongest synoptic-scale storms [82] and highest electricity demand (data from EIA). Highly erosive periods are more evenly distributed across all calendar months in the NE, but peak in late fall early winter, which is displaced from the summer peak in electricity demand (data from EIA) (Figure 7a).

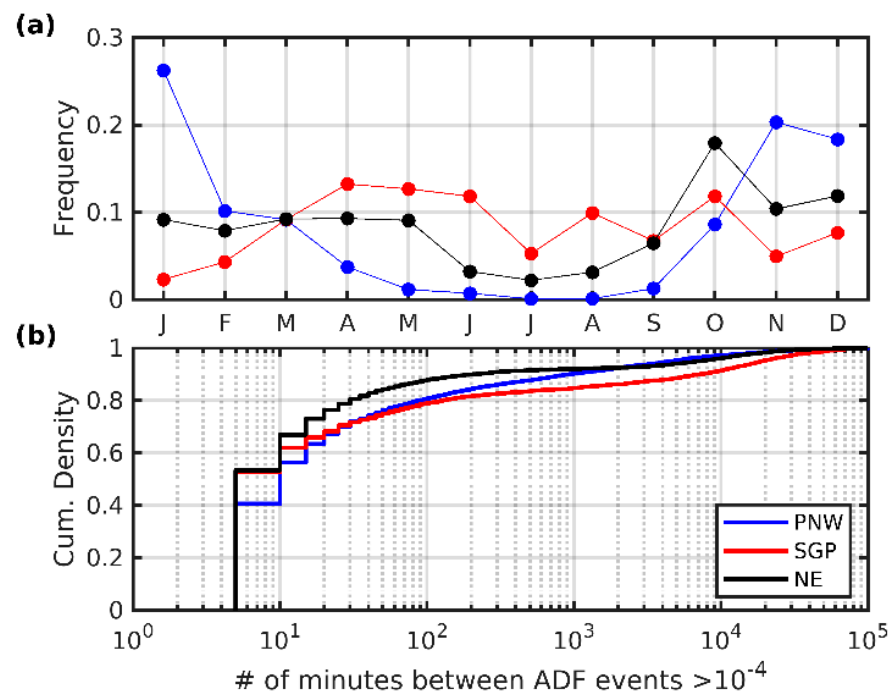


Figure 7. Temporal variability of blade coating accumulated distance to failure increments ($ADFi$). (a) Seasonality of occurrence of 5-min ADF increments $> 1 \times 10^{-4}$ and (b) the cumulative density function (CDF) of the time interval between consecutive periods with 5-min ADF increments $> 1 \times 10^{-4}$ for the exemplar sites in the Pacific Northwest (PNW), Southern Great Plains (SGP), and Northeastern US (NE) (see site locations in Figure 2b).

An additional matter of importance for the possible use of erosion-safe mode to reduce LEE is the concentration of highly erosive periods in time. Over half of periods

with ADF increments $> 1 \times 10^{-4}$ at the SGP and NE occur in consecutive 5-min periods (Figure 7b). Run length statistics suggest that 99% of time periods with continuous ADF increments $> 1 \times 10^{-4}$ have durations in the SGP of less than one hour. This implies that substantial increments in total coating ADF are contributed not only by relatively few 5-min periods, but also by those periods being highly concentrated in time. This finding would suggest a very high economic value in short-term meteorological forecasting of highly erosive events to inform decisions regarding the implementation of erosion-safe mode and hence derating of wind farms to extend blade lifetimes. It also suggests high economic value in on site measurements of precipitation characteristics in addition to wind speeds in site pre-construction assessments.

In accord with expectations, 18-year ADF computed using larger numbers of years of meteorological observations increasingly converge on best estimate values derived from all 18-years of data (Figure 8). Estimates of 18-year ADF, and hence blade coating lifetime, are also a function of the precise calendar years included particularly at sites where ADF_t is very heavy tailed (Figure 8b). For data records spanning 5 years, the minimum to maximum range of 18-year ADF estimates, derived using draws of different calendar year combinations, is 0.44 (PNW), 0.58 (SGP), and 0.39 (NE) of the 18-year ADF estimates derived using the entire data record (Figure 8). The blade coating lifetime for the PNW site computed using the most erosive 5 calendar years is 6.3 years, while the coating lifetime for the least erosive 5 years is 10 years. The best estimate of coating lifetime computed using the entire data record is 7.6 years. Equivalent estimates for the SGP are 9.6 (most erosive 5 years), 20 (least erosive 5 years), and 13 years (entire data record). Those for the NE site are 6.3, 8.9, and 7.5 years, respectively. For data records comprising 15 calendar years, the minimum to maximum range of 18-year ADF estimates is narrower with values of 0.12 (PNW), 0.18 (SGP), and 0.10 (NE) of estimates derived using the entire data record. This analysis affirms the value of using long-duration, high-frequency meteorological data in computing blade coating lifetime estimates particularly for sites in the SGP where ADF increments are concentrated in time.

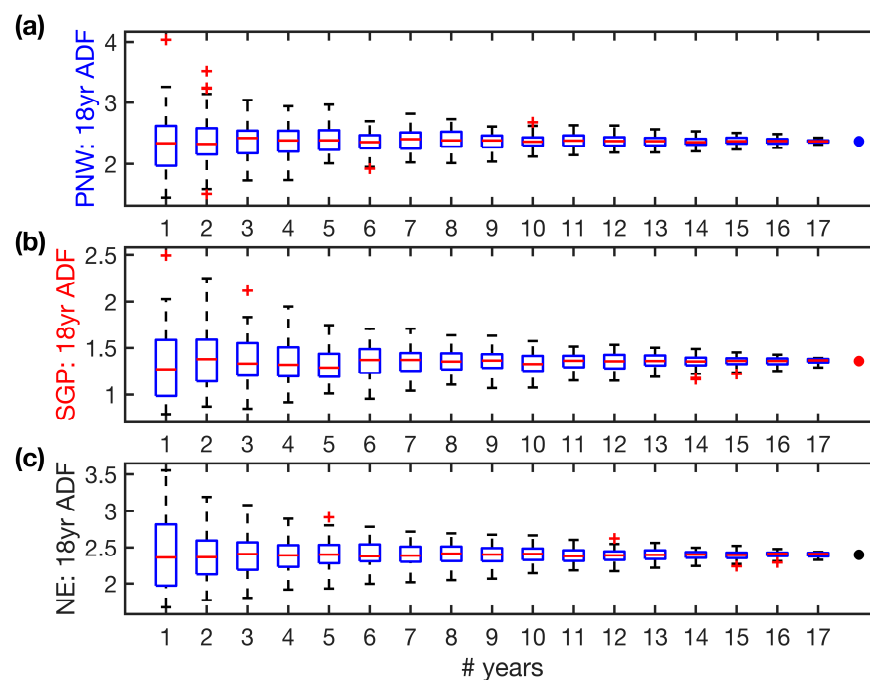


Figure 8. Boxplots of 18-year ADF estimates at (a) PNW, (b) SGP, and (c) NE ASOS stations derived using meteorological records of different durations (1–17 years). Each sample draw comprises different individual years selected without replacement. Also shown is the 18-year ADF derived using the longest record available (point at far right of each panel).

Eighteen-year ADF across the ASOS sites scales positively with both annual total precipitation and mean wind speeds (Figure 9a,b). However, consistent with the non-linear codependence of ADF on wind speed *and* rainfall rate (Figure 4) and the concentration of ADF increments in time (Figures 5b, 6 and 7b), annual mean wind speed and total precipitation are relatively poor predictors of the spatial variability of modelled 18-year ADF at sites across the CONUS. For example, 18 ASOS stations have an average annual total precipitation of 1000 ± 10 mm, and the 18-year ADF at those locations range from 0.26 to 1.33. Less than 29% of the station-to-station variance in 18-year ADF is explained by annual total precipitation, and <22% is explained by the mean wind speeds (Figure 9a,b).

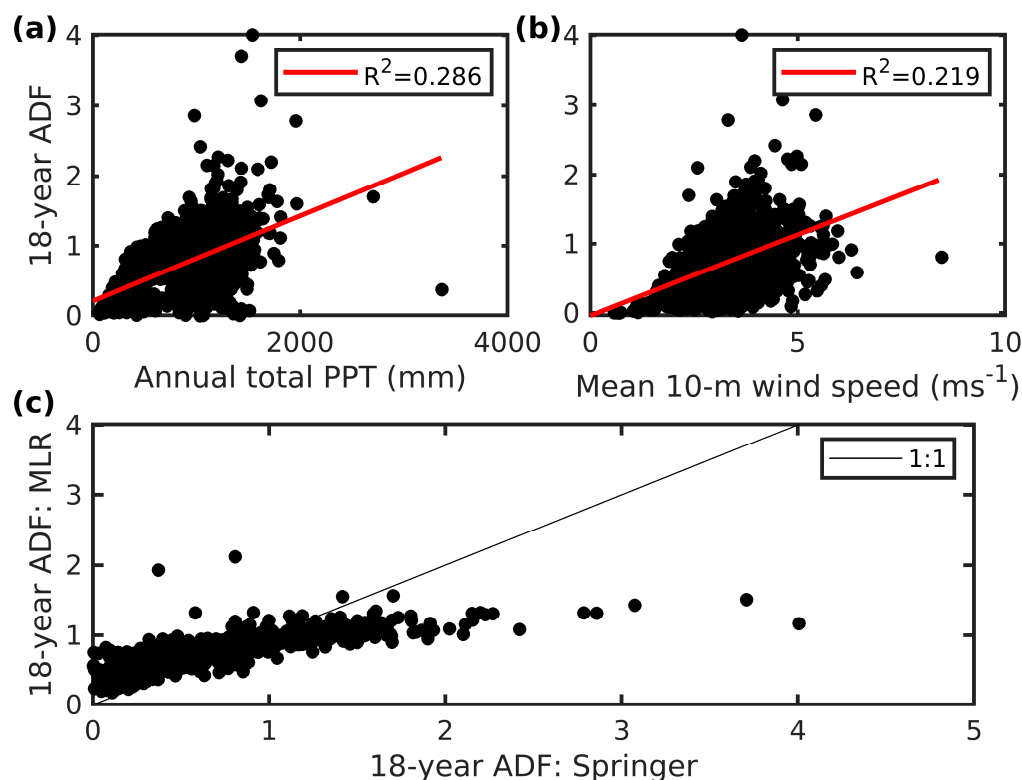


Figure 9. Relationship between blade coating lifetime and the primary meteorological drivers. Scatterplots of 18-year ADF versus (a) annual total precipitation and (b) mean 10-m wind speed at the ASOS stations. Red line indicates a linear regression fit ($18\text{yrADF} = c_0 + c_1 \times x$), where x is either annual total precipitation (PPT) or mean wind speed, and the c_0 and c_1 are the regression coefficients (all are significantly different from zero at $p = 0.01$). The variance explanation (R^2) of each of the regression fits, adjusted for sample size, is given in the legends. (c) Scatterplot of predictions of 18-year ADF derived using Equation (16) (MLR) versus the 18-year ADF at each site as derived using the detailed meteorological data and the Springer model.

A multiple linear regression model of 18-year ADF as a function of mean annual total precipitation (PPT) and a dependency on mean wind speed squared (WS^2) to capture the non-linear dependence of tip speed on wind speed (Figure 1a) with forced zero has an R^2 (variance explanation) of 0.55. In addition, the coefficients are statistically different from zero at $p = 0.01$ (i.e., 99% confidence level):

$$18\text{yrADF} = 0.0273 \times \text{WS}^2 + 5.2310^{-4} \times \text{PPT} \quad (16)$$

However, this best fit equation does not capture the dynamic range of 18-year ADF across the CONUS (Figure 8c). This analysis demonstrates the importance of using a more

mechanistic model such as Springer with high-frequency meteorological data in assessing blade coating lifetimes.

3.4. Uncertainties in Blade Coating Lifetimes

This is the first geospatial description of wind turbine blade leading edge erosion potential to be generated for the CONUS and as such represents a substantial advancement in the state of knowledge and a new tool for the wind energy industry. The atlas is publicly available and predicated on both a transparent and repeatable methodology and the use of a high-fidelity federal dataset of meteorological observations with high time resolution.

The modeled estimates of blade coating 18-year ADF, and hence likelihood of onset of blade erosion, are subject to some caveats. The resolution of the ASOS wind speed and precipitation data necessarily impacts the ADF estimates provided here. Further, as shown, the record length of the meteorological observations and the precise years sampled are also important in dictating 18-year ADF and blade lifetimes (Figure 8). Particularly, at sites with a high concentration of ADF_t in specific events, there is a need to employ long-duration time series. The absolute values of 18-year ADF are also a function of the coefficients used in the Springer model [79], and it is important to acknowledge that the coefficient values are selected to be conservative [46] and may, therefore, overestimate blade coating lifetimes. The use of alternative HSD approximations would also change the absolute values of 18-year ADF (Figure 4). However, it is likely that the spatial patterns and gradients would be substantially unchanged if different model parameters were applied. The modeling presented herein further assumes an impingement efficiency of 1 for all hydrometeor diameters. The DNV RP uses an approximation of impingement efficiency (β) as a function of hydrometeor diameter (D) that is derived from experiments in an icing research tunnel simulating icing on aircraft wings [83]. It has the following form:

$$\beta = 1 - e^{-15D} \quad (17)$$

where D is in mm. This approximation yields impingement efficiencies > 0.99 for $D > 0.3$ mm. Introduction of this correction to the number of blade impacts changes the example 5-min increments in ADF shown in Figure 4a by $< 0.3\%$. Thus, corrections for impingement efficiency for smaller hydrometeors that may be deflected from the blade has a negligible impact on coating lifetimes.

The spatial variability in estimated blade coating lifetimes (described using ADF) presented here are consistent with the limited past research available for the CONUS [46]. Assessment of the reliability of this geospatial analysis would greatly benefit from the availability of data from wind farm owner-operators or wind turbine manufacturers regarding observed coating damage from their wind turbine fleets deployed across North America. While ASOS is the premier meteorological network in the USA, blade lifetime estimates derived using different models of material stress and/or meteorological datasets (observational or derived using numerical weather prediction models) would be a useful supplement to the information provided here.

An important caveat to the current research pertains to hail as a damage vector. The material's response to hail impacts is generally larger than those from rain (liquid) droplets [36,84–88]. Thus, the 18-year ADF estimates in regions such as the Southern Great Plains that have a high hail frequency (Figure 2a) [72,73] are likely to be negatively biased. With the currently available ASOS data, it is not possible to correct coating lifetimes for the potential effects of hail.

4. Concluding Remarks

Wind turbine blade leading edge erosion negatively impacts wind farm economics via decreased energy production (AEP) and increased operations and maintenance (O&M) costs. O&M costs are also a primary source of uncertainty in projections for future LCoE from wind energy [6]. While there are options to reduce LEE, the selection of an optimal solution in each location requires detailed information regarding the causes, magnitude, and spatiotemporal variability in damage accumulation. Hence, there is value in generating and applying a robust method to yield spatiotemporally explicit estimates of blade coating accumulated distance to failure (ADF) and hence erosion onset estimates.

Despite the caveats identified in Section 3.4, it is expected that the geospatial variability in relative blade coating lifetimes presented herein are relatively robust. These 18-year coating ADF estimates, computed using conservative estimates of material properties, illustrate large spatial gradients with one-quarter of locations indicating coating failure within <18 years, short of the expected wind turbine lifetime of ~30 years [89]. Many sites with high ADF estimates are in coastal locations and/or in the central CONUS, which have the highest density of wind turbine assets (cf. Figures 2a and 5).

While previous research has sought to derive estimates of wind turbine blade coating lifetimes for Danish Seas [90], northern European Seas [91], and the Netherlands [92], to the authors knowledge this is the first geospatial description of blade coating lifetimes for the USA and the first to explicitly address temporal variability of blade coating ADF increments (ADF_t). The high-frequency damage increments derived from the modeling presented here permit important insights into the relative concentration of ADF in time, the degree to which material stress is focused on consecutive periods, and the seasonality of highly erosive periods (Figures 6 and 7). This information is valuable in assessing where LEE reduction might best be achieved via adoption of erosion-safe mode and where, conversely, implementation of leading edge protective measures is economical. For regions with current/near future high densities of wind turbine installations, the ADF of blade coatings is most concentrated in time in the Southern Great Plains and is much less concentrated in time in either the Pacific Northwest or along the US east coast (Figure 6). One-third of the blade coating lifetime is expended at the SGP site during the 360 most erosive 5-min periods (or 30 h) (Figure 6). Hence, erosion-safe mode enacted during just a few minutes per year may substantially slow the progress toward coating failure and the initiation of erosion. Thus, erosion-safe mode is likely to be the most effective as a LEE mitigation measure in this region rather than incurring the cost and loss of AEP associated with the use of LEP products. Conversely, over three times as many of the highest erosive periods are required to expend 33% of the coating lifetime (i.e., achieve the $ADF = 0.33$ threshold) at the representative site in the Pacific Northwest. Hence, cost-effective solutions to elongate blade coating lifetimes in this region may involve the use of LEP products.

Author Contributions: Conceptualization, S.C.P. and R.J.B.; methodology, S.C.P. and R.J.B.; software, S.C.P.; validation, S.C.P. and R.J.B.; formal analysis, S.C.P.; investigation, S.C.P., J.J.C., and R.J.B.; resources, S.C.P.; data curation, S.C.P. and J.J.C.; writing—original draft preparation, S.C.P. and R.J.B.; writing—review and editing, S.C.P., J.J.C., and R.J.B.; visualization, S.C.P.; supervision, S.C.P.; project administration, S.C.P. and R.J.B.; funding acquisition, S.C.P. and R.J.B. All authors have read and agreed to the published version of the manuscript.

Funding: This research was funded by the U.S. National Science Foundation (2329911), Sandia National Laboratory (DE-NA0003525), and U.S. Department of Energy (DE-SC0016605). Computational resources used in these analyses are provided by the NSF Extreme Science and Engineering Discovery Environment (XSEDE2) (award TG-ATM170024).

Data Availability Statement: Data from the National Weather Service Automated Surface Observing System network are available for download from: <https://www.ncei.noaa.gov/products/land-based-station/automated-surface-weather-observing-systems> (last accessed 14 November 2024). Data from the NASA Passive Microwave Hail Climatology Data Products V1 dataset shown in Figure 2 are available for download from: <https://search.earthdata.nasa.gov/> (last accessed 21 July 2022). The LEE atlas for CONUS can be downloaded from ZENODO, doi: 10.5281/zenodo.14247620.

Acknowledgments: The authors gratefully acknowledge the scientists and engineers responsible for the ASOS network and the comments of two anonymous reviewers.

Conflicts of Interest: The authors declare no conflicts of interest.

References

1. Barthelmie, R.J.; Pryor, S.C. Potential contribution of wind energy to climate change mitigation. *Nat. Clim. Change* **2014**, *4*, 684–688. [CrossRef]
2. Barthelmie, R.J.; Pryor, S.C. Climate Change Mitigation Potential of Wind Energy. *Climate* **2021**, *9*, 136. [CrossRef]
3. GWEC. *Global Wind Report 2024*; Global Wind Energy Council: Brussels, Belgium, 2024; p. 168. Available online: <https://gwec.net/global-wind-report-2024/> (accessed on 5 September 2024).
4. Lazard. Lazard's Levelized Cost of Energy Analysis—Version 16.0; Zurich, Switzerland; 2023. Available online: <https://www.lazard.com/research-insights/levelized-cost-of-energyplus/> (accessed on 5 September 2024).
5. Xu, J.; Zou, J.; Ziegler, A.D.; Wu, J.; Zeng, Z. What drives the change of capacity factor of wind turbine in the United States? *Environ. Res. Lett.* **2023**, *18*, 064009. [CrossRef]
6. Wisler, R.; Rand, J.; Seel, J.; Beiter, P.; Baker, E.; Lantz, E.; Gilman, P. Expert elicitation survey predicts 37% to 49% declines in wind energy costs by 2050. *Nat. Energy* **2021**, *6*, 555–565. [CrossRef]
7. Enevoldsen, P.; Xydis, G. Examining the trends of 35 years growth of key wind turbine components. *Energy Sustain. Dev.* **2019**, *50*, 18–26. [CrossRef]
8. Bolinger, M.; Wisler, R.; O'Shaughnessy, E. Levelized cost-based learning analysis of utility-scale wind and solar in the United States. *iScience* **2022**, *25*, 104378. [CrossRef] [PubMed]
9. Wisler, R.H.; Bolinger, M.; Lantz, E. Assessing wind power operating costs in the United States: Results from a survey of wind industry experts. *Renew. Energy Focus* **2019**, *30*, 46–57. [CrossRef]
10. Brøndsted, P.; Nijssen, R.P.; Goutianos, S. *Advances in Wind Turbine Blade Design and Materials*; Woodhead Publishing: Cambridge, UK, 2023.
11. Du, Y.; Zhou, S.; Jing, X.; Peng, Y.; Wu, H.; Kwok, N. Damage detection techniques for wind turbine blades: A review. *Mech. Syst. Signal Process.* **2020**, *141*, 106445. [CrossRef]
12. Liu, D.; da Fonseca, L.G. *Global Onshore Wind Power Operations & Maintenance (O&M) 2020*; Wood Mackenzie: Edinburgh, UK, 2021. Available online: <https://www.woodmac.com/reports/power-markets-global-onshore-wind-power-operations-and-maintenance-oandm-2020-467883/> (accessed on 5 September 2024).
13. Mishnaevsky, L., Jr.; Thomsen, K. Costs of repair of wind turbine blades: Influence of technology aspects. *Wind. Energy* **2020**, *23*, 2247–2255. [CrossRef]
14. Mishnaevsky Jr, L.; Frost-Jensen Johansen, N.; Fraisse, A.; Fæster, S.; Jensen, T.; Bendixen, B. Technologies of wind turbine blade repair: Practical comparison. *Energies* **2022**, *15*, 1767. [CrossRef]
15. Sun, S.; Wang, T.; Yang, H.; Chu, F. Damage identification of wind turbine blades using an adaptive method for compressive beamforming based on the generalized minimax-concave penalty function. *Renew. Energy* **2022**, *181*, 59–70. [CrossRef]
16. Santelo, T.N.; de Oliveira, C.M.R.; Maciel, C.D.; de Monteiro, A.J.R.B. Wind turbine failures review and trends. *J. Control Autom. Electr. Syst.* **2022**, *33*, 505–521. [CrossRef]
17. Ozturk, S.; Fthenakis, V. Predicting frequency, time-to-repair and costs of wind turbine failures. *Energies* **2020**, *13*, 1149. [CrossRef]
18. Pryor, S.C.; Barthelmie, R.J.; Coburn, J.J.; Zhou, X.; Rodgers, M.; Norton, H.; Campobasso, M.S.; López, B.M.; Hasager, C.B.; Mishnaevsky Jr, L. Prioritizing Research for Enhancing the Technology Readiness Level of Wind Turbine Blade Leading-Edge Erosion Solutions. *Energies* **2024**, *17*, 6285. [CrossRef]
19. Maniaci, D.C.; MacDonald, H.; Paquette, J.; Clarke, R. *Leading Edge Erosion Classification System*; Technical Report from IEA Wind Task 46 Erosion of Wind Turbine Blades; Sandia National Lab: Albuquerque, NM, USA, 2022; 52p. Available online: <https://iea-wind.org/task46/t46-results/> (accessed on 5 September 2024).
20. Mishnaevsky Jr, L.; Hasager, C.B.; Bak, C.; Tilg, A.-M.; Bech, J.I.; Rad, S.D.; Fæster, S. Leading edge erosion of wind turbine blades: Understanding, prevention and protection. *Renew. Energy* **2021**, *169*, 953–969. [CrossRef]
21. Sareen, A.; Sapre, C.A.; Selig, M.S. Effects of leading edge erosion on wind turbine blade performance. *Wind Energy* **2014**, *17*, 1531–1542. [CrossRef]

22. Gaudern, N. A practical study of the aerodynamic impact of wind turbine blade leading edge erosion. *J. Phys. Conf. Ser.* **2014**, *524*, 012031. [CrossRef]
23. Froese, M. Wind-farm owners can now detect leading-edge erosion from data alone. *Windpower Engineering and Development*, 14 August 2018. Available online: <https://www.windpowerengineering.com/wind-farm-owners-can-now-detect-leading-edge-erosion-from-data-alone/> (accessed on 5 September 2024).
24. Campobasso, M.S.; Castorrini, A.; Ortolani, A.; Minisci, E. Probabilistic analysis of wind turbine performance degradation due to blade erosion accounting for uncertainty of damage geometry. *Renew. Sustain. Energy Rev.* **2023**, *178*, 113254. [CrossRef]
25. Xiaoxun, Z.; Xinyu, H.; Xiaoxia, G.; Xing, Y.; Zixu, X.; Yu, W.; Huaxin, L. Research on crack detection method of wind turbine blade based on a deep learning method. *Appl. Energy* **2022**, *328*, 120241. [CrossRef]
26. Kong, K.; Dyer, K.; Payne, C.; Hamerton, I.; Weaver, P.M. Progress and trends in damage detection methods, maintenance, and data-driven monitoring of wind turbine blades—A review. *Renew. Energy Focus* **2023**, *44*, 390–412. [CrossRef]
27. DNV. *DNV-RP-0573 Evaluation of Erosion and Delamination for Leading Edge Protection Systems of Rotor Blades*; Det Norske Veritas: Høvik, Norway, 2021; 44p.
28. Lopez, J.C.; Kolios, A.; Wang, L.; Chiachio, M.; Dimitrov, N. Reliability-based leading edge erosion maintenance strategy selection framework. *Appl. Energy* **2024**, *358*, 122612. [CrossRef]
29. Law, H.; Koutsos, V. Leading edge erosion of wind turbines: Effect of solid airborne particles and rain on operational wind farms. *Wind Energy* **2020**, *23*, 1955–1965. [CrossRef]
30. Boopathi, K.; Mishnaevsky Jr, L.; Sumantraa, B.; Premkumar, S.A.; Thamodharan, K.; Balaraman, K. Failure mechanisms of wind turbine blades in India: Climatic, regional, and seasonal variability. *Wind Energy* **2022**, *25*, 968–979. [CrossRef]
31. Walzberg, J.; Cooperman, A.; Watts, L.; Eberle, A.L.; Carpenter, A.; Heath, G.A. Regional representation of wind stakeholders' end-of-life behaviors and their impact on wind blade circularity. *iScience* **2022**, *25*, 104734. [CrossRef] [PubMed]
32. Bech, J.I.; Hasager, C.B.; Bak, C. Extending the life of wind turbine blade leading edges by reducing the tip speed during extreme precipitation events. *Wind Energy Sci.* **2018**, *3*, 729–748. [CrossRef]
33. Bartolomé, L.; Teuwen, J. Prospective challenges in the experimentation of the rain erosion on the leading edge of wind turbine blades. *Wind Energy* **2019**, *22*, 140–151. [CrossRef]
34. Zhang, S.; Dam-Johansen, K.; Nørkjær, S.; Bernad, P.L., Jr.; Kiil, S. Erosion of wind turbine blade coatings—design and analysis of jet-based laboratory equipment for performance evaluation. *Prog. Org. Coat.* **2015**, *78*, 103–115. [CrossRef]
35. Pryor, S.C.; Barthelmie, R.J.; Cadence, J.; Dellwik, E.; Hasager, C.B.; Kral, S.T.; Reuder, J.; Rodgers, M.; Veraart, M. Atmospheric Drivers of Wind Turbine Blade Leading Edge Erosion: Review and Recommendations for Future Research. *Energies* **2022**, *15*, 8553. [CrossRef]
36. Letson, F.; Barthelmie, R.J.; Pryor, S.C. RADAR-derived precipitation climatology for wind turbine blade leading edge erosion. *Wind Energy Sci.* **2020**, *5*, 331–347. [CrossRef]
37. Doagou-Rad, S.; Mishnaevsky Jr, L. Rain erosion of wind turbine blades: Computational analysis of parameters controlling the surface degradation. *Meccanica* **2020**, *55*, 725–743. [CrossRef]
38. Verma, A.S.; Castro, S.G.; Jiang, Z.; Teuwen, J.J. Numerical investigation of rain droplet impact on offshore wind turbine blades under different rainfall conditions: A parametric study. *Compos. Struct.* **2020**, *241*, 112096. [CrossRef]
39. Tempelis, A.; Jespersen, K.M.; Mishnaevsky, L., Jr. Fatigue damage mechanics approach to predict the end of incubation and breakthrough of leading edge protection coatings for wind turbine blades. *Int. J. Fatigue* **2025**, *190*, 108617. [CrossRef]
40. Rinker, J.; Dykes, K.L. *WindPACT Reference Wind Turbines*; NREL/TP-5000-67667; National Renewable Energy Lab. (NREL): Golden, CO, USA, 2018. Available online: <https://www.nrel.gov/docs/fy18osti/67667.pdf> (accessed on 5 September 2024).
41. Gunn, R.; Kinzer, G.D. The terminal velocity of fall for water droplets in stagnant air. *J. Atmos. Sci.* **1949**, *6*, 243–248. [CrossRef]
42. Marshall, J.S.; Palmer, W.M.K. The distribution of raindrops with size. *J. Meteorol.* **1948**, *5*, 165–166. [CrossRef]
43. Best, A. The size distribution of raindrops. *Q. J. R. Meteorol. Soc.* **1950**, *76*, 16–36. [CrossRef]
44. Springer, G.S.; Baxi, C.B. A model for rain erosion of homogeneous materials. In *Erosion, Wear, and Interfaces with Corrosion*; ASTM International: West Conshohocken, PA, USA, 1974; pp. 106–124.
45. Springer, G.S.; Yang, C.-I.; Larsen, P.S. Analysis of rain erosion of coated materials. *J. Compos. Mater.* **1974**, *8*, 229–252. [CrossRef]
46. Letson, F.; Pryor, S.C. From Hydrometeor Size Distribution Measurements to Projections of Wind Turbine Blade Leading Edge Erosion. *Energies* **2023**, *5*, 3906. [CrossRef]
47. Johnston, B.; Foley, A.; Doran, J.; Littler, T. Levelised cost of energy, A challenge for offshore wind. *Renew. Energy* **2020**, *160*, 876–885. [CrossRef]
48. Đukan, M.; Gumber, A.; Egli, F.; Steffen, B. The role of policies in reducing the cost of capital for offshore wind. *iScience* **2023**, *26*, 106945. [CrossRef] [PubMed]
49. Hoen, B.D.; Diffendorfer, J.E.; Rand, J.T.; Kramer, L.A.; Garrity, C.P.; Hunt, H.E. *United States Wind Turbine Database (v6.1, November 2023)*; U.S. Geological Survey, American Clean Power Association, and Lawrence Berkeley National Laboratory Data Release; United States Geological Survey: Reston, VA, USA, 2018.

50. Rand, J.T.; Kramer, L.A.; Garrity, C.P.; Hoen, B.D.; Diffendorfer, J.E.; Hunt, H.E.; Spears, M. A continuously updated, geospatially rectified database of utility-scale wind turbines in the United States. *Sci. Data* **2020**, *7*, 15. [CrossRef]
51. Bang, S.D.; Cecil, D.J. Constructing a multifrequency passive microwave hail retrieval and climatology in the GPM domain. *J. Appl. Meteorol. Climatol.* **2019**, *58*, 1889–1904. [CrossRef]
52. Mishnaevsky Jr, L.; Tempelis, A.; Kuthe, N.; Mahajan, P. Recent developments in the protection of wind turbine blades against leading edge erosion: Materials solutions and predictive modelling. *Renew. Energy* **2023**, *215*, 118966. [CrossRef]
53. Frost-Jensen Johansen, N.; Mishnaevsky Jr, L.; Dashtkar, A.; Williams, N.A.; Fæster, S.; Silvello, A.; Cano, I.G.; Hadavinia, H. Nanoengineered graphene-reinforced coating for leading edge protection of wind turbine blades. *Coatings* **2021**, *11*, 1104. [CrossRef]
54. Fæster, S.; Johansen, N.F.J.; Mishnaevsky Jr, L.; Kusano, Y.; Bech, J.I.; Madsen, M.B. Rain erosion of wind turbine blades and the effect of air bubbles in the coatings. *Wind Energy* **2021**, *24*, 1071–1082. [CrossRef]
55. Herring, R.; Dyer, K.; Martin, F.; Ward, C. The increasing importance of leading edge erosion and a review of existing protection solutions. *Renew. Sustain. Energy Rev.* **2019**, *115*, 109382. [CrossRef]
56. Ansari, Q.M.; Sánchez, F.; Mishnaevsky, L., Jr.; Young, T.M. Evaluation of offshore wind turbine blades coating thickness effect on leading edge protection system subject to rain erosion. *Renew. Energy* **2024**, *226*, 120378. [CrossRef]
57. Major, D.; Palacios, J.; Maughmer, M.; Schmitz, S. Aerodynamics of leading-edge protection tapes for wind turbine blades. *Wind Eng.* **2021**, *45*, 1296–1316. [CrossRef]
58. Katsivalis, I.; Chanteli, A.; Finnegan, W.; Young, T.M. Mechanical and interfacial characterisation of leading-edge protection materials for wind turbine blade applications. *Wind Energy* **2022**, *25*, 1758–1774. [CrossRef]
59. Coburn, J.J.; Pryor, S.C. Projecting future energy production from operating wind farms in North America: Part 3: Variability. *J. Appl. Meteorol. Climatol.* **2023**, *62*, 1523–1537. [CrossRef]
60. Jeon, H.; Hartman, B.; Cutler, H.; Hill, R.; Hu, Y.; Lu, T.; Shields, M.; Turner, D.D. Estimating the economic impacts of improved wind speed forecasts in the United States electricity sector. *J. Renew. Sustain. Energy* **2022**, *14*, 036101. [CrossRef]
61. Huff, F. Time distribution characteristics of rainfall rates. *Water Resour. Res.* **1970**, *6*, 447–454. [CrossRef]
62. Huff, F.A.; Neill, J.C. Frequency of point and areal mean rainfall rates. *Eos Trans. Am. Geophys. Union* **1956**, *37*, 679–681.
63. Kursinski, A.L.; Zeng, X. Areal estimation of intensity and frequency of summertime precipitation over a midlatitude region. *Geophys. Res. Lett.* **2006**, *33*, L22401. [CrossRef]
64. Cook, N.J. Locating the anemometers of the US ASOS network and classifying their local shelter. *Weather* **2022**, *77*, 256–263. [CrossRef]
65. McNitt, J.A.; Facundo, J. An overview of the Federal Government’s Automated Surface Observing System sustainment activity. In Proceedings of the 13th American Meteorological Society Conference on Integrated Observing and Assimilation Systems for Atmosphere, Oceans, and Land Surface, Phoenix, AZ, USA, 11–15 January 2009.
66. Cook, N.J. Curating the TD6405 database of 1-min interval wind observations across the USA for use in Wind Engineering studies. *J. Wind. Eng. Ind. Aerodyn.* **2022**, *224*, 104961. [CrossRef]
67. Schmitt, I.V.; Chester, V. A quality control algorithm for the ASOS ice free wind sensor. In Proceedings of the 13th American Meteorological Society Conference on Integrated Observing and Assimilation Systems for Atmosphere, Oceans, and Land Surface, Phoenix, AZ, USA, 11–15 January 2009.
68. National Oceanic Atmospheric Administration. *Automated Surface Observing System (ASOS) User’s Guide*; National Oceanic Atmospheric Administration: Silver Spring, MD, USA, 1998.
69. Butler, R.D.; McKee, T.B. *ASOS Heated Tipping Bucket Performance Assessment and Impact on Precipitation Climate Continuity*; Libraries: NASA 19990025176; Colorado State University: Fort Collins, CO, USA, 1998; Available online: <https://apps.dtic.mil/sti/citations/ADA359136> (accessed on 5 September 2024).
70. White, S.G.; Winans, L.J.; Fiore Jr, J.V. Development of the all-weather precipitation accumulation gauge for ASOS. In Proceedings of the American Meteorological Society Eighth Symposium on Integrated Observing and Assimilation Systems for Atmosphere, Oceans, and Land Surface, Seattle, WA, USA, 11–15 January 2004.
71. Irwin, J.S. A theoretical variation of the wind profile power-law exponent as a function of surface roughness and stability. *Atmos. Environ.* **1979**, *13*, 191–194. [CrossRef]
72. Letson, F.; Shepherd, T.J.; Barthelmie, R.J.; Pryor, S.C. WRF modelling of deep convection and hail for wind power applications. *J. Appl. Meteorol. Climatol.* **2020**, *59*, 1717–1733. [CrossRef]
73. Pryor, S.; Letson, F.; Shepherd, T.; Barthelmie, R. Evaluation of WRF simulation of deep convection in the US Southern Great Plains. *J. Appl. Meteorol. Climatol.* **2023**, *62*, 41–62. [CrossRef]
74. Pryor, S.C.; Barthelmie, R.J. Wind shadows impact planning of large offshore wind farms. *Appl. Energy* **2024**, *359*, 122755. [CrossRef]
75. Eisenberg, D.; Laustsen, S.; Stege, J. Wind turbine blade coating leading edge rain erosion model: Development and validation. *Wind Energy* **2018**, *21*, 942–951. [CrossRef]
76. Castorrini, A.; Venturini, P.; Bonfiglioli, A. Generation of Surface Maps of Erosion Resistance for Wind Turbine Blades under Rain Flows. *Energies* **2022**, *15*, 5593. [CrossRef]
77. Springer, G.S. *Erosion by Liquid Impact*; John Wiley and Sons: New York, NY, USA, 1976; p. 278.

78. Herring, R.; Domenech, L.; Renau, J.; Šakalytė, A.; Ward, C.; Dyer, K.; Sánchez, F. Assessment of a wind turbine blade erosion lifetime prediction model with industrial protection materials and testing methods. *Coatings* **2021**, *11*, 767. [[CrossRef](#)]
79. Hoksbergen, N.; Akkerman, R.; Baran, I. The Springer model for lifetime prediction of wind turbine blade leading edge protection systems: A review and sensitivity study. *Materials* **2022**, *15*, 1170. [[CrossRef](#)] [[PubMed](#)]
80. Villarini, G.; Smith, J.A.; Baeck, M.L.; Marchok, T.; Vecchi, G.A. Characterization of rainfall distribution and flooding associated with US landfalling tropical cyclones: Analyses of Hurricanes Frances, Ivan, and Jeanne (2004). *J. Geophys. Res. Atmos.* **2011**, *116*, D23116. [[CrossRef](#)]
81. Brauer, N.S.; Basara, J.B.; Homeyer, C.R.; McFarquhar, G.M.; Kirstetter, P.E. Quantifying precipitation efficiency and drivers of excessive precipitation in post-landfall Hurricane Harvey. *J. Hydrometeorol.* **2020**, *21*, 433–452. [[CrossRef](#)]
82. Mass, C. *The Weather of the Pacific Northwest*; University of Washington Press: Lanham, MD, USA, 2021; 312p, ISBN 9780295748443.
83. Papadakis, M.; Wong, S.-C.; Rachman, A.; Hung, K.E.; Vu, G.T.; Bidwell, C.S. *Large and Small Droplet Impingement Data on Airfoils and Two Simulated Ice Shapes*; NASA, Report #E-15275; Glenn Research Center: Cleveland, OH, USA, 2007. Available online: <https://ntrs.nasa.gov/citations/20070034950> (accessed on 5 September 2024).
84. Heymsfield, A.; Szakáll, M.; Jost, A.; Giammanco, I.; Wright, R. A comprehensive observational study of graupel and hail terminal velocity, mass flux, and kinetic energy. *J. Atmos. Sci.* **2018**, *75*, 3861–3885. [[CrossRef](#)]
85. Keegan, M.H.; Nash, D.; Stack, M. On erosion issues associated with the leading edge of wind turbine blades. *J. Phys. D Appl. Phys.* **2013**, *46*, 383001. [[CrossRef](#)]
86. Kim, H.; Kedward, K.T. Modeling hail ice impacts and predicting impact damage initiation in composite structures. *AIAA J.* **2000**, *38*, 1278–1288. [[CrossRef](#)]
87. Macdonald, J.; Stack, M. Some thoughts on modelling hail impact on surfaces. *J. Bio-Tribo-Corros.* **2021**, *7*, 1–7. [[CrossRef](#)]
88. Zhu, X.; Fu, X.; Liu, L.; Xu, K.; Luo, G.; Zhao, Z.; Chen, W. Damage mechanism of composite laminates under multiple ice impacts at high velocity. *Int. J. Impact Eng.* **2022**, *168*, 104296. [[CrossRef](#)]
89. Wisner, R.H.; Bolinger, M. *Benchmarking Anticipated Wind Project Lifetimes: Results from a Survey of US Wind Industry Professionals*; Berkeley Lab, Electricity Markets and Policy Group: San Francisco, CA, USA, 2019. Available online: <https://emp.lbl.gov/publications/benchmarking-anticipated-wind-project> (accessed on 5 September 2024).
90. Hasager, C.; Vejen, F.; Bech, J.; Skrzypiąski, W.; Tilg, A.-M.; Nielsen, M. Assessment of the rain and wind climate with focus on wind turbine blade leading edge erosion rate and expected lifetime in Danish Seas. *Renew. Energy* **2020**, *149*, 91–102. [[CrossRef](#)]
91. Hannesdóttir, Á.; Kral, S.T.; Reuder, J.; Hasager, C.B. Rain erosion atlas for wind turbine blades based on ERA5 and NORA3 for Scandinavia. *Results Eng.* **2024**, *22*, 102010. [[CrossRef](#)]
92. Bartolomé, L.; Teuwen, J. Methodology for the energetic characterisation of rain erosion on wind turbine blades using meteorological data: A case study for The Netherlands. *Wind Energy* **2021**, *24*, 686–698. [[CrossRef](#)]

Disclaimer/Publisher’s Note: The statements, opinions and data contained in all publications are solely those of the individual author(s) and contributor(s) and not of MDPI and/or the editor(s). MDPI and/or the editor(s) disclaim responsibility for any injury to people or property resulting from any ideas, methods, instructions or products referred to in the content.

Appendix B: An erosion atlas of Scandinavia

Reference: Hannesdóttir Á., Kral S. T., Reuder J. and Hasager C. B. (2024): Rain erosion atlas for wind turbine blades based on ERA5 and NORA3 for Scandinavia. *Results in Engineering*, 22, 102010. Reproduced with kind permission of the publisher.

Rain erosion atlas for wind turbine blades based on ERA5 and NORA3 for Scandinavia

Hannesdóttir et al.

Methodology

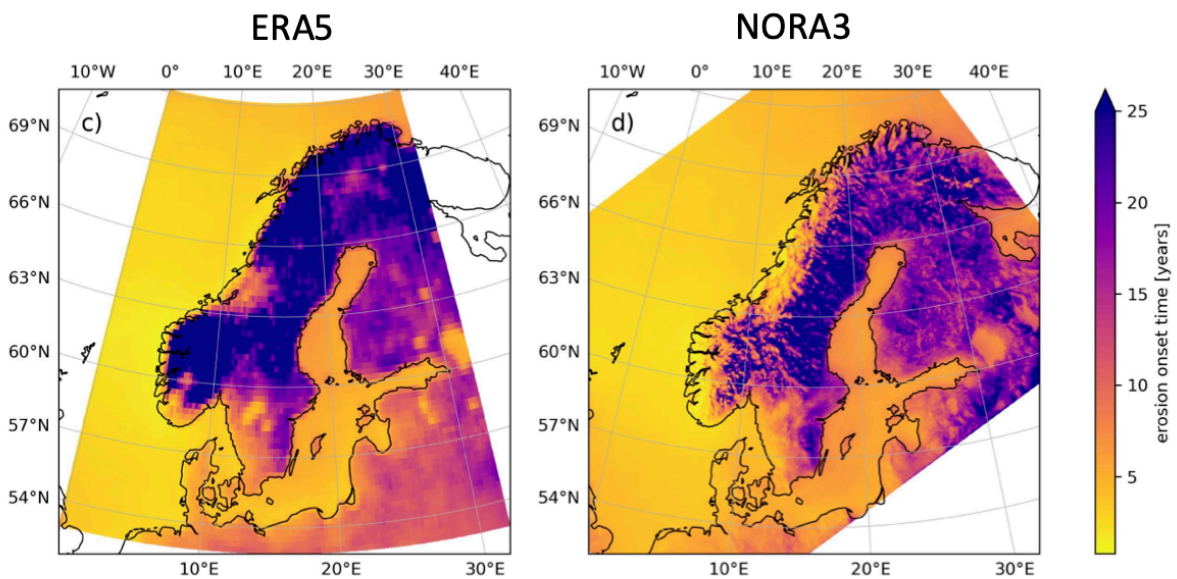
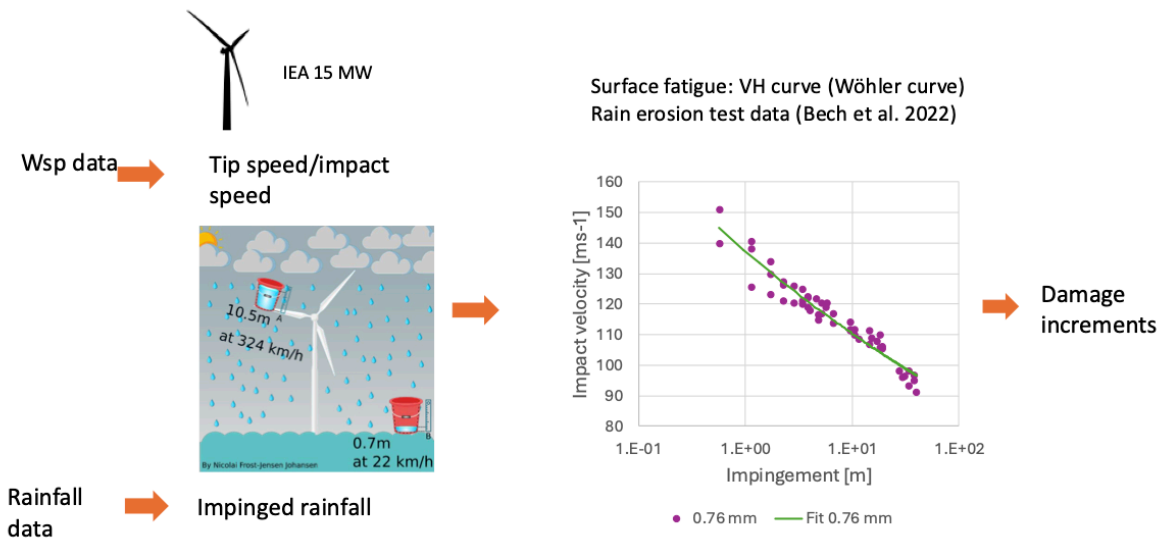
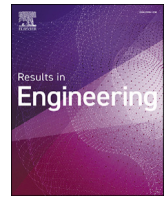


Figure 4 Summary of the methodology and the coating lifetime estimates for Scandinavia.



Research paper



Rain erosion atlas for wind turbine blades based on ERA5 and NORA3 for Scandinavia

Ásta Hannesdóttir^a, Stephan T. Kral^{b,*}, Joachim Reuder^b, Charlotte Bay Hasager^{a,b}

^a Department of Wind and Energy Systems, Technical University of Denmark, Frederiksborgvej 399, 4000, Roskilde, Denmark

^b Geophysical Institute and Bergen Offshore Wind Centre, University of Bergen and Bjerkes Centre for Climate Research, Allegaten 70, N-5007, Bergen, Norway

ARTICLE INFO

Keywords:

Rain erosion atlas
Wind turbine blade coating
Precipitation and wind
Empirical damage model
Impingement to end of incubation
Offshore conditions

ABSTRACT

Leading edge erosion on wind turbine blades is a common issue, particularly for wind turbines placed in regions characterized by high wind speeds and precipitation. This study presents the development of a rain erosion atlas for Scandinavia and Finland, based on ERA5 reanalysis and NORA3 mesoscale model data on rainfall intensity and wind speed over five years. The IEA 15 MW reference wind turbine is used as an example to evaluate impingement water impact and erosion onset time for a commercial coating material. The damage progression is modeled by combining the wind speed and rainfall data with an empirical damage model that relates impinged water (H) as a function of impact velocity to the time of erosion onset. Comparative analyses at two weather station locations show that NORA3 data more accurately aligns with measurements in terms of power spectral density, mean wind speed, rainfall, and erosion prediction than ERA5. NORA3-based atlas layers offer finer spatial detail and predict shorter erosion onset times over land compared to ERA5, particularly in complex terrain. Conversely, the ERA5-based atlas suggests a shorter onset of erosion offshore. Based on NORA3 data, erosion onset time is estimated at 5 years on average for Baltic Sea wind farm sites and 3.2 years for sites in the North Sea.

1. Introduction

Leading edge erosion (LEE) at wind turbine blades is the damage of the surface of the blades due to environmental impacts [1,2], where rain is one of the dominant contributors. The cost for repair of blades due to erosion is considerable [3] and therefore there is a focus on understanding blade erosion, prevention, protection [4], and mapping the environmental factors leading to erosion and areas that have heightened risk of erosion [5] and damage progression.

Damage progression in blade coating materials are assessed in rain erosion tests following a recommended practice [6]. The tests involve high-speed rotation of blade material specimens on a whirling arm under needles dropping similar-sized droplets. Damage progression and lifetime predictions are based on factors like time, amount of water hitting the specimens, and impact speed. Recent advancements include droplet-size dependent lifetime prediction and comparisons between different testing methods [7].

The connecting links between rain erosion tests and real atmospheric conditions are 1) the speed of the specimen versus the tip speed

of a turbine in operation, and 2) the droplet impact at the specimen in the rain erosion tester versus the multitude of droplets impact to the leading edge of the blades.

Studies on the relationship between atmospheric conditions and the risk of LEE have been explored. Some studies include observed damage at blades and atmospheric model rain data output for different climate zones in Europe [8–10]. Other studies include the prediction of blade lifetime based on local meteorological rain and wind observations from weather stations in Denmark [11], Germany [12], and the Netherlands [13,14]. Common to the studies based on local weather observations is that the results indicate a higher risk for erosion at coastal compared to inland sites. In the USA, a study based on weather radar data for a region in the Mid-West prone to severe hail show high LEE risk due to hail [15]. In Europe, hail prevails frequently in central and southern regions but lesser at high latitudes and offshore [16]. Satellite-based rain data used for the prediction of blade lifetime at sites in Denmark, Germany, and Portugal [17] yield lifetimes similar to those based on situ rain data for most of the sites.

* Corresponding author.

E-mail address: stephan.kral@uib.no (S.T. Kral).

In recent decades, numerous wind energy related atlases have been developed, ranging from regional to global scales. These atlases typically map the available wind resources [18–21] or siting parameters for wind turbines [22], aiding in project preparation and planning. They serve to identify areas of interest and potential risk prior to project initiation. However, despite the existence of these atlases, there remains a notable research gap concerning the mapping of rain erosion risk for wind turbine blades on a larger scale. To address this gap, we propose a methodology that integrates numerical simulations of environmental conditions with a rain erosion damage model. In this research we utilize ERA5 [23], a global reanalysis model, and NORA3 [24], a mesoscale hindcasting model, to construct the first rain erosion atlas for Scandinavia.

The specific aim of the study is to provide the first rain erosion atlas for wind turbine blades covering Scandinavian and Finland based on numerical simulations of the environmental conditions and compare the simulation-based results to selected weather stations. The first objective is to assess the usability of ERA5 reanalysis data compared to NORA3 mesoscale model output for this specific purpose. ERA5 has the advantage of global coverage, while NORA3 has a superior spatial resolution making it a suitable candidate to investigate LEE in more complex terrain. First, a comparison of rain data from ERA5, NORA3, and two selected weather stations representing offshore conditions is performed. Second, an evaluation of the power spectra on wind speed and rainfall intensity for ERA5 and NORA3 versus weather station data is done to characterize the scales resolved by the models. Third, the turbine-specific information from one turbine types (IEA 15 MW) is combined with the spray mode VH-curve from the coating system tested in rain erosion test [7] and the results comprise an assessment of the impingement water and damage increments from ERA5, NORA3 and weather station data at two coastal sites. Finally, the rain erosion atlas using ERA5 and NORA3 is calculated for the IEA 15 MW turbine for the entire study area and the two resulting atlases are compared.

The second objective is to evaluate the results with a particular aim for offshore wind farm sites, where precipitation observations are sparse or non-existing. At the same time the risk of erosion is considerable at these sites.

The paper is structured as follows: Section 2 presents the data sources ERA5, NORA3, and weather station data and method using the damage model calculation for a reference wind turbine. Section 3 presents results starting with a comparison of the model and measurement data, including spectral analysis and statistical results for two measurement sites. Finally, the rain erosion atlases based on ERA5 and NORA3 are presented together with more detailed results for some existing or planned offshore sites. Section 4 contains the discussion and Section 5 conclusions.

2. Data and methodology

In this section, we describe the dataset used in the study and the methodology of the rain erosion calculation method.

2.1. Impingement model for damage calculations

The impingement of precipitation on turbine blades in operation causes gradual leading-edge erosion damage over time. The damage model we use in our study is based on rain erosion test data which is described in detail in Bech et al. [7]. The rain erosion tests are performed using a Rain Erosion Tester (RET) developed by R&D Test Systems A/S. This equipment contains a three-bladed rotor with one specimen per blade and can achieve rotor speeds of up to 1386 rpm. The rain field is created using needles that dispense water droplets of varying sizes and fall velocities, with the standard flow ensuring droplet formation by gravitational force and surface tension. During testing, images are taken at regular intervals to track erosion on the specimens. The collected data, after visual inspection analysis, depicts erosion as a function

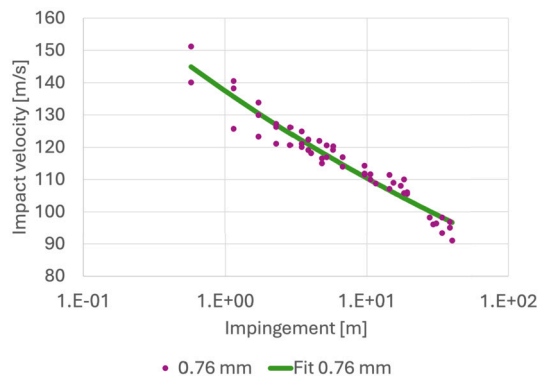


Fig. 1. Data points and fitted VH curve for end of incubation of the rain erosion test in spray mode.

of time and position. The onset of visible erosion in the RET images indicates the initial failure of the protective coating. When this happens it is called the erosion onset time, or in other words, the incubation time. The damage typically starts near the high-velocity rotor tip and progresses inward. To quantify damage progression, the data is fitted to a power law function, called a VH curve, correlating the rotor velocity (V) to the impinged water column (H):

$$H(V) = H_0 \left(\frac{V}{V_0} \right)^{-m} \quad (1)$$

where H_0 and m are parameters found from fitting the curve to data using the least-squares method and $V_0 = 1 \text{ m/s}$ is a normalization velocity.

Fig. 1 shows the RET data and fitted VH curve we use in our study. Each data point shows when the end of incubation is reached and erosion onset has started for a given impact velocity and impinged water. We can see from the figure that for an impact velocity of 110 m/s we will need 10 m of impinged water for erosion onset.

The fitted parameters we use in our study are $H_0 = 2.85 \times 10^{22} \text{ m}$ and $m = 10.5$, which have been estimated from RET data where the needles were in spray mode, giving a broad distribution of droplet sizes (average droplet diameter of 76 μm) and fall velocities. The top coating that was used on the test specimens is a commercial polyurethane coating that is used on some modern wind turbine blades with relatively good erosion resistance.

2.2. Damage calculations from meteorological data

When using the impingement model with meteorological data, we need to convert measured or modeled rainfall data to impinged water on the blade tip by

$$h(U, I) = \frac{I}{V_{fall}(I)} V_{tip}(U) \Delta t \quad (2)$$

where I is the rainfall intensity in m/s, V_{fall} is the fall velocity of the rain droplets, V_{tip} is the tip speed of the wind turbine blade, Δt is the time step of the data in seconds, and U is the horizontal wind speed at hub height. This is done for every time step in the data time series. As the fall velocity of the rain droplets is not known in our study, it is derived from an empirical relation of droplet distribution and terminal velocities as a function of rainfall intensity [25]. The tip speed is found from a tip-speed curve as a function of wind speed at hub height. Here we use the IEA 15 MW reference wind turbine [26], which has a hub height of 150 m, blade length of 117 m, and maximum tip speed of 95 m/s (see more parameters in Table 1).

Damage calculations are based on the Palmgren-Miner rule [27], and an estimate of accumulated damage is obtained by

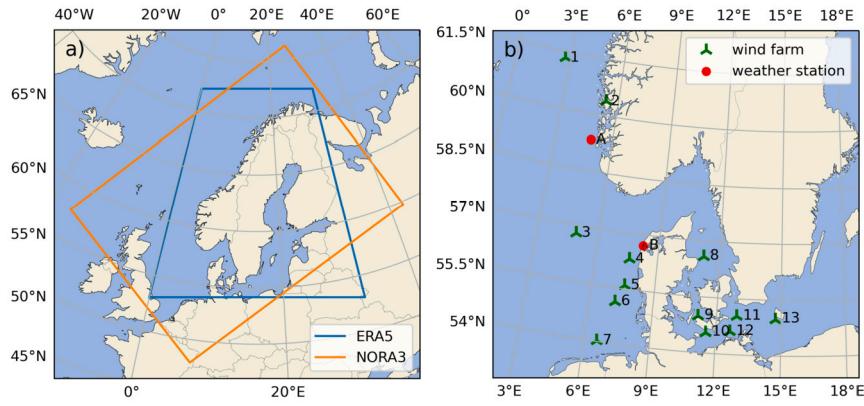


Fig. 2. a) A map of the selected domains of ERA5 data and NORA3 data. b) Locations of weather stations (red) and wind farms (green).

Table 1

The main parameters of the IEA 15 MW turbine.

IEA 15 MW	
Rotor diameter	240 m
Blade length	117 m
Cut-in wind speed	3 m/s
Rated wind speed	10.59 m/s
Cut-out wind speed	25 m/s
Minimum rotor speed	5 rpm
Maximum rotor speed	7.56 rpm
Minimum tip speed	62.83 m/s
Maximum tip speed	95 m/s
Hub height	150 m

$$D = \sum_{i=1}^k \frac{h_i(U_i, I_i)}{H_i(V_{rel})} \quad (3)$$

where k is the number of time steps and $V_{rel} = \sqrt{V_{tip}^2 + U^2}$ is the velocity of droplets relative to the blade.¹ The accumulated damage describes the onset of rain erosion when $D = 1$, i.e. the end of incubation and the initial failure of the coating due to liquid precipitation. Solid hydrometers such as hail were not included in the RET and are therefore not taken into account by this modeling framework.

2.3. ERA5 reanalysis data

Wind speeds and precipitation from the “ERA5 hourly data on single levels from 1959 to present” provided by the European Union’s Copernicus service are used. ERA5 is the fifth generation of the European Centre for Medium-Range Weather Forecast (ECMWF) atmospheric reanalysis of the global climate [23]. The dataset has an hourly temporal resolution and the spatial resolution is 0.25° which is equivalent to ~30 km horizontal resolution. We use the wind speed at 150 m (the hub height of the IEA 15 MW turbine) and total precipitation with a flag for liquid precipitation only. The ERA5 dataset has a spatial domain with global coverage, but for this study, we have selected a subdomain covering Scandinavia, from 53° to 72° latitude and between 0° and 32° longitude. The border of the selected ERA5 spatial subdomain is indicated with a blue line in Fig. 2 a). The selected 5-year time period for this study is from 1 January 2015 to 31 December 2019.

2.4. NORA3 mesoscale data

NORA3, the 3-km Norwegian Reanalysis, is a mesoscale atmospheric hindcast dataset for the Norwegian Sea, the North, and the Barents

¹ the vertical velocity component of the droplets is averaged out during the time step due to the rotation of the blade.

Sea, currently covering the time period from 1969 to 2023 [24]. It is dynamically downscaled from ERA5 reanalysis using the HARMONIE-AROME model, providing atmospheric fields on a 3-km spatial resolution. NORA3 includes a convection-permitting non-hydrostatic model that resolves mesoscale features, thus it is expected to provide superior performance on precipitation compared to ERA5. A one-hour time resolution is achieved by deterministic forecasts every 6 hours with lead times from 3 to 9 hours for near-surface parameters. The 3-hour lead time output serves as a reference for the conversion of accumulated parameters, which are summed up from the start of each forecast. For a good overlap with ERA5 for the area of interest, we limit our analyses to a subdomain of NORA3 spanned by 57.72°N, -16.47°E; 48.02°N, 6.97°E; 59.87°N, 42.41°E; and 76.30°N, 26.33°E: In this study, we make use of the 1h-mean horizontal wind speed at an assumed hub height of 150 m, interpolated from the nearest available output levels at 100 m and 250 m, and the accumulated precipitation parameters. To achieve the highest level of comparability between ERA5 and NORA3 we decided to focus on liquid precipitation only. Thus we compute the mean-hourly rain rate as the difference between the total accumulated precipitation amount (NORA3 parameter: *precipitation_amount_acc*) and the total accumulated solid precipitation (*snowfall_amount_acc*) minus the corresponding value from the previous lead time.

2.5. Weather station data at two selected sites

Observations from two coastal weather stations, Thyborøn in Denmark and Utsira Fyr in Norway (Fig. 2 b), are used for comparison to the ERA5 and NORA3 data for wind speed and rainfall. These two sites were selected since the corresponding data sets of precipitation and wind observations are sufficiently long and have a high enough time resolution for a model evaluation. Furthermore, they represent two separate sites that can be considered as representative of coastal and offshore conditions in suspectedly erosion-prone areas. The Utsira data covers a period from 2016-03-15 to 2019-03-15 while the Thyborøn time series is longer, from 2015-01-01 to 2019-12-31. Both weather station datasets have a 10-minute temporal resolution and the measurement height is 10 m for wind speed.

We calculate the power spectral density of the wind speed and rainfall intensity to analyze the variability at different frequencies. The spectral density of a measured time series (x) is estimated by

$$S_x(f) = \frac{1}{N f_s} |\hat{x}|^2 \quad (4)$$

where f is the frequency, f_s is the sampling frequency, N is the number of measurements in the time series, and \hat{x} is the discrete Fourier transform of x .

Table 2

Statistics and rain erosion damage model results at the weather stations Utsira and Thyborøn based on measured data, ERA5 and NORA3. The relative differences to the observations are given in parentheses. The average wind speed values from the measurements are extrapolated to the 150 m-level (marked with an asterisk).

#	Weather station	Data source	Average wind speed [m/s]	Average annual rainfall [mm]	Average annual impinged water [m]	Erosion onset time [years]
A	Utsira	Meas.	9.58*	1319	22.32	2.49
		ERA5	9.33 (-2.6%)	1626 (+23.3%)	34.53 (+54.7%)	1.69 (-32.1%)
		NORA3	9.57 (-0.1%)	1240 (-6.0%)	23.63 (+5.9%)	2.34 (-5.8%)
B	Thyborøn	Meas.	8.44*	843	12.89	6.48
		ERA5	9.40 (+11.3%)	964 (+14.4%)	20.97 (+62.8%)	3.04 (-53.0%)
		NORA3	9.68 (+14.7%)	870 (+3.2%)	17.17 (+33.3%)	3.44 (-46.9%)

As the damage model uses hub height wind speed as an input, we use extrapolated 10 m wind speeds for the comparison with the modeled data. The extrapolation is done to 150 m with the power law:

$$U(z) = U_{ref} \left(\frac{z}{z_{ref}} \right)^\alpha \tag{5}$$

where U_{ref} and z_{ref} are the reference wind speed and height (10 m) respectively and α is the shear exponent. Note that there is a considerable uncertainty involved with vertical extrapolation of this kind, due to changes in the shear exponent with time, height, wind direction, and atmospheric stability. However, we choose this approach for simplicity. For the Utsira wind data, we use $\alpha = 0.063$ based on Peña et al. [28] where the shear exponent has been estimated at Utsira. To the authors' knowledge, the shear exponent has not been estimated at Thyborøn, so we use an estimate of $\alpha = 0.077$ from Høvsøre [29] which is a nearby site. More details about the weather station data can be found in Hasager et al. [12].

3. Results

3.1. Analysis of data at two weather station sites

In this section, we compare the measured wind speed and rainfall data with the modeled data and the calculated damages at the two weather stations Utsira and Thyborøn. The model data time series are selected from the nearest grid points of the two sites.

The smoothed power spectral density of the time series can be seen in Fig. 3. The smoothing is done so that 15 estimates appear in each decade, mainly smoothing the spectrum in the high-frequency range. Here it can be noticed that the measured time series extend to higher frequencies than both models due to the higher temporal resolution of the measured data. The spectral slope of the measured wind speed and NORA3 wind speed is close to the theoretical slope in the inertial range of $f^{-5/3}$ for frequencies above 2 day^{-1} (Fig. 3 a) and b)). For comparison, the ERA5 wind speed spectra have a much steeper slope due to the lower spatial resolution of the data. Note that a grid cell covers a $3 \times 3 \text{ km}^2$ in NORA3, whereas in ERA5 a grid cell corresponds to an area of approximately $30 \times 13 \text{ km}^2$.

Similarly, we see in Fig. 3 c) and d) that the rain intensity spectra for ERA5 have a higher spectral slope in the high-frequency range. The spectral slope of the NORA3 rain intensity follows the slope of the measurements better, especially at Thyborøn (Fig. 3 d)).

Table 2 shows the annual average wind speed at 150 m height and average annual rainfall at the weather stations and the corresponding nearest grid cell in ERA5 and NORA3. The calculated mean annual values of impinged water and erosion onset time are listed as well as the relative difference to the measured data. Note that for Utsira, the period covered is from 2016-03-15 to 2019-03-15, and for Thyborøn from 2015-01-01 to 2019-12-31. The period is limited by available weather station measurements from met.no and DMI for direct comparison between models and measurements.

The comparison of wind speeds at the coastal station Utsira shows good agreement of both reanalysis products to the vertically extrapolated wind speed from the observations, with ERA5 wind speed being

slightly lower (Table 2). At Thyborøn, both models have a larger positive wind speed bias compared to the observations. However, here it should be noted that the wind speed measurements at Thyborøn are influenced by nearby buildings that give an increased roughness and reduced wind speeds for some periods, resulting in data values at and close to 0 m/s.

At Utsira, the average annual measured rainfall is much closer to NORA3 than to ERA5 with a relative bias of -6% and +23%, respectively. At Thyborøn, the picture is similar, with both NORA3 (+3%) and ERA5 (+14%) showing positive deviations.

For the average annual impinged water and erosion onset time, both resulting from the wind speed and rainfall data, both models indicate a higher amount of impinged water for both locations and correspondingly earlier erosion onset times compared to the measurements. In general, NORA3 shows a better agreement with the reference and the spread between the models is much larger at Utsira than at Thyborøn, with ERA5 indicating the onset of erosion already after 1.7 years at Utsira. The earlier onset time at Utsira from NORA3 may, at first sight, appear counterintuitive, since the annual rainfall is less compared to the observations, whereas the average wind speeds are almost identical. In this case, the resulting values are caused by a higher correlation between rain events and periods of high wind speeds in NORA3 than in the measurements.

Fig. 4 shows the cumulative rain at Utsira (a) and Thyborøn (b) and the corresponding modeled damage increments (c and d). Comparing the measured rain with NORA3 we see that for some periods the rain is underestimated and other periods overestimated, but the final cumulative rainfall is comparable. ERA5 rainfall is overestimated more regularly. At Utsira the picture for the cumulative damage increments is similar with a much better agreement between the observations and NORA3 (Fig. 4 c)). However, at Thyborøn both models agree better in terms of the cumulative damage increments, with clearly higher values than the observations (Fig. 4 d)). Parts of this behavior can be attributed to the wind speed measurements not being representative during all times as mentioned above.

3.2. Rain Erosion Atlas Layers based on ERA5 and NORA3

Fig. 5 shows the annual mean rainfall from ERA5 data a) and from NORA3 b) and the mean wind speed at 150 m height.

When comparing the ERA5 layers with NORA3 we see greater details in both wind and rain fields, especially in the mountain areas. The area experiencing the highest amount of annual precipitation lies on the west coast of Norway. For ERA5 this area extends offshore, while for the NORA3 rain, it is confined onshore along the coast. The mean wind speed over land in complex terrain is known to be underestimated in ERA5 [24], likely due to enhanced surface roughness, and we can clearly see this for the mean wind field at 150 m when comparing Fig. 5 c) and d). The ERA5 mean wind speeds over Norway are the lowest wind speeds on the whole map, while in NORA3 the wind speeds in the same area show some distinct peaks due to speedup effects over the mountains.

The annual accumulated impinged water/rainfall of the IEA 15 MW wind turbine can be seen in Fig. 6 based on ERA5 data in a) and based

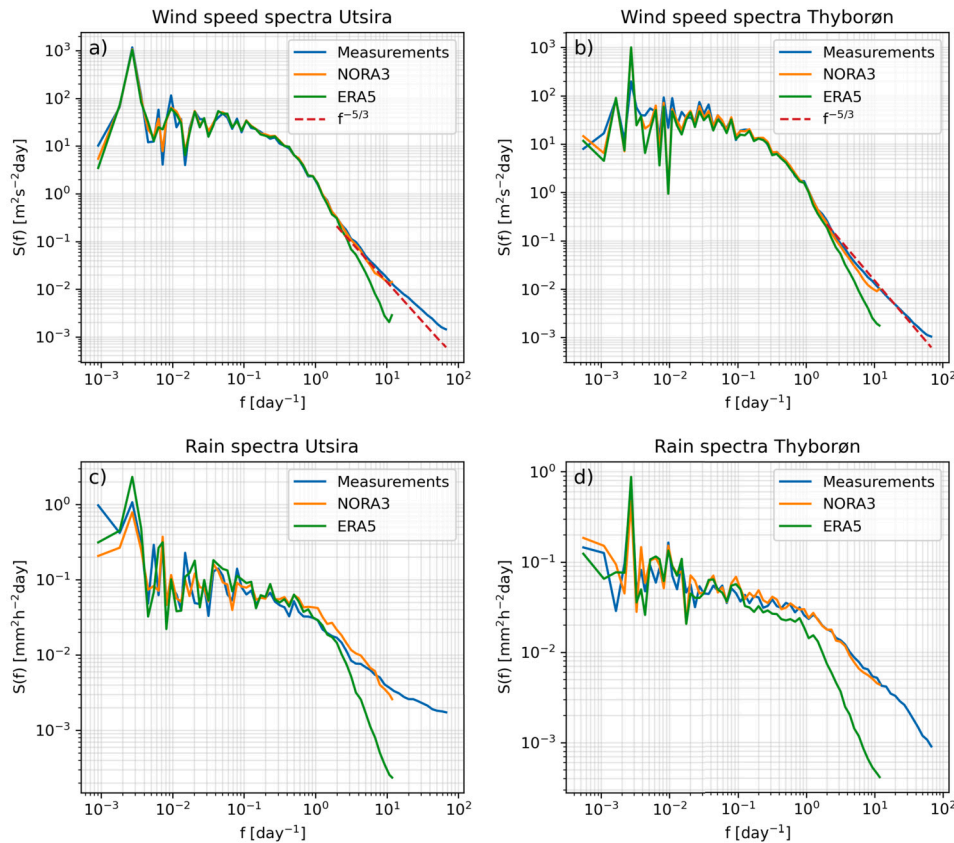


Fig. 3. Wind speed and rainfall intensity power spectrum comparing measurement, NORA3 and ERA5 at Utsira (Norway) and Thyborøn (Denmark). The theoretical spectral slope line $f^{-5/3}$ is shown for higher frequency wind speed.

on NORA3 data in b). We see that the highest values of impinged water on the map can reach 40 m and above. The amount of impinged water that the tip of the blade will encounter in a year depends on the wind speed, rainfall, and wind turbine tip speed (of the assumed wind turbine model), but is independent of the blade material. However, for the onset time of erosion, the impinged water amount has been coupled with the VH curve of a commercial blade material. Fig. 6 c) and d) show the onset time of erosion for the IEA 15 MW wind turbine with the assumed commercial material based on ERA5 and NORA3 data, respectively. The maximum onset time of the color scale is limited to 25 years, which is a typical lifetime of wind turbine components.

We see that the offshore areas have the highest amount of accumulated impinged water and the shortest onset time of erosion. The main difference between the erosion onset time for NORA3 and ERA5 are that the short onset times extend further inland in Norway for the NORA3 data, due to the higher amount of modeled rainfall and higher wind speed on the west coast of Norway.

3.3. Focus on offshore areas

Fig. 7 shows the onset time of rain erosion where the land areas have been masked out and the color scale is limited to 5 years. This is done to have a better view of the variation in incubation time over the offshore areas. Comparing the prediction based on ERA5 a) to NORA3 b), it can be seen that the predicted erosion onset time is shortest along the westward coastal lines for the ERA5 dataset. This coastal effect can not be seen in the erosion onset time based on the NORA3 dataset and the predicted damage onset are generally at later times for the offshore areas in NORA3.

Table 3 lists the values of the different atlas layers (Fig. 5 and Fig. 6) extracted at wind farm sites in the Norwegian and the North Seas (henceforth called North Sea). The location and the numbering of

the wind farm sites can be seen in Fig. 2 b). The results are based on model data of the time period from 01.01.2015 to 31.12.2019 (5 years). It is shown in section 3.1 that NORA3 is closer to the measured rainfall than ERA5. Thus, to be consistent with the calculation of the relative bias, we choose to normalize with NORA3.

The average wind speeds at the North Sea offshore sites are 10.2 m/s in ERA5 and 10.3 m/s in NORA3. For offshore sites, the average relative bias in wind speeds is minimal with -0.6%, i.e., the wind speed in NORA3 is slightly higher than in ERA5 at 150 m. The only exception is the inland site Bergen, which has a lower wind speed (≈ 6.3 m/s) than the offshore sites.

The average annual rainfall at the North Sea sites has a relative bias of 19.8%. ERA5 estimates higher average annual rainfall (1004 mm) than NORA3 (839 mm). On average, ERA5 is 165 mm wetter than NORA3. ERA5 shows a positive bias at all sites. Both models indicate the highest rainfall at the northernmost offshore site and the lowest rainfall at the southernmost offshore site. In Bergen, located inland, the average annual rainfall in both models is very high (>2200 mm).

Results for the six offshore wind farm sites in the Inner Danish and Baltic Seas (henceforth called Baltic Sea) are listed in Table 4. Average wind speeds in ERA5 (9.4 m/s) and NORA3 (9.5 m/s) compare well with a relative bias of -0.9%. At EnBW Baltic, an absolute difference of 0.7 m/s (relative bias -7.2%) is noted. The average annual rainfall in ERA5 (715 mm) is larger than in NORA3 (622 mm). ERA5 is, on average, 93 mm wetter than NORA3 (relative bias of 15.0%).

In summary, ERA5 and NORA3 compare well for wind speeds data in the Baltic Sea, while ERA5 shows higher precipitation levels than NORA3. The Baltic Sea is characterized by lower wind speeds and lesser rainfall than the North Sea. Consequently, the average onset time for erosion at wind farm sites in the Baltic Sea is longer. Based on NORA 3, erosion onset time is estimated to be 5 years in Baltic Sea locations and 3.2 years in North Sea sites.

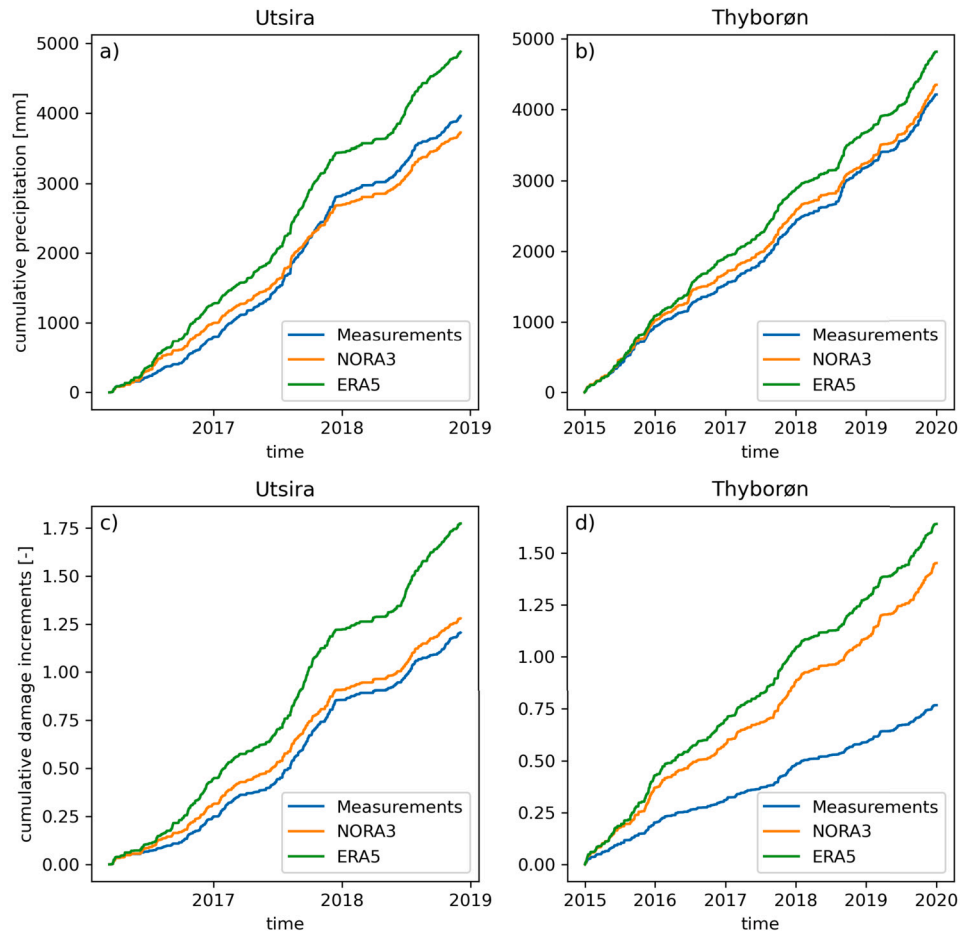


Fig. 4. Cumulative rainfall comparing measurement, NORA3 and ERA5 at Utsira (Norway) and Thyborøn (Denmark). The time period is matched with the available measurements.

Table 3

Average wind speed at 150 m, annual average rainfall and impinged water, and erosion onset time at North Sea sites (see Fig. 5), based on ERA5 and NORA3, and for the IEA 15 MW wind turbine with a commercial blade coating.

#	Wind farm site	Data source	Average wind speed [m/s]	Average annual rainfall [mm]	Average annual impinged water [m]	Erosion onset time [years]
1	Hywind Tampen	ERA5	10.2	1342	29.8	1.8
		NORA3	10.6	1151	23.3	2.2
2	Bergen Florida	ERA5	5.9	2548	45.1	2.1
		NORA3	6.7	2209	38.3	1.8
3	Sørlige Nordsjø II	ERA5	10.5	935	21.8	2.5
		NORA3	10.6	799	16.6	3.1
4	Thor	ERA5	10.4	967	22.4	2.5
		NORA3	10.3	806	16.6	3.3
5	Horns Rev II	ERA5	10.2	901	21.0	2.7
		NORA3	10.2	765	15.9	3.4
6	Dan Tysk	ERA5	10.2	939	21.8	2.6
		NORA3	10.2	765	15.9	3.4
7	Alpha Ventus	ERA5	9.9	942	22.1	2.6
		NORA3	9.9	745	15.2	3.7
Offshore Averages		ERA5	10.2	1004	23.2	2.4
		NORA3	10.3	839	17.2	3.2
		Rel. bias	-0.6%	19.8%	34.3%	-23.5%

Offshore regions are here generally identified as critical areas for rain erosion. For a turbine of a similar size of the IEA 15 MW, the commercial blade material coating assessed in this study would start to erode within the first quarter of the expected turbine lifetime. We observe that there is a considerable variation in predicted erosion onset times in the offshore areas. Wind farm locations in the Baltic Sea and inner Danish seas exhibit significantly longer erosion onset times

compared to those in the North Sea. Furthermore, the maps in Fig. 7 highlight the offshore areas along the southwest coast of Norway as the most critical regions for rain erosion.

4. Discussion

Our study presents a complete rain erosion atlas for wind turbine blades in Scandinavia and adjacent offshore regions. As this is the first

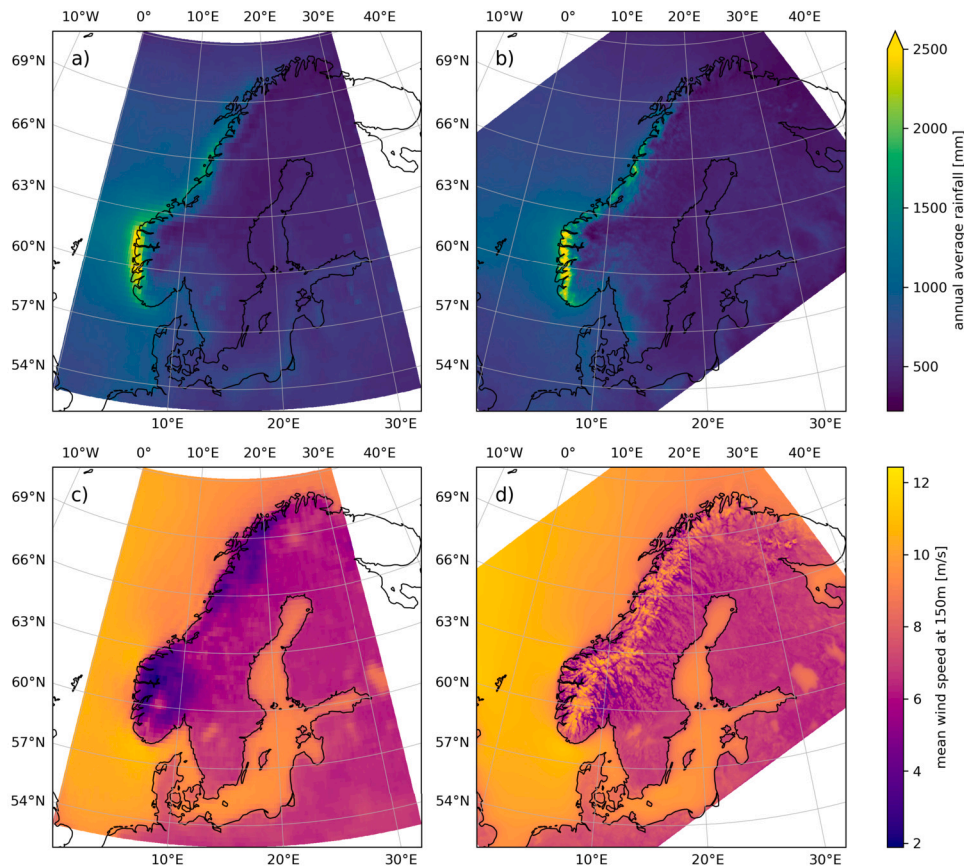


Fig. 5. The annual average rainfall for a) ERA5, b) NORA3 and average wind speed at 150 m for c) ERA5 and d) NORA3.

Table 4

Average wind speed at 150 m, annual average rainfall and impinged water, and erosion onset time at Baltic Sea sites (see Fig. 5), based on ERA5 and NORA3, and for the IEA 15 MW wind turbine with a commercial blade coating.

#	Wind farm site	Data source	Average wind speed [m/s]	Average annual rainfall [mm]	Average annual impinged water [m]	Erosion onset time [years]
8	Anholt	ERA5	9.6	761	17.6	3.4
		NORA3	9.6	678	13.7	4.4
9	Vindeby	ERA5	9.5	727	16.5	3.8
		NORA3	9.1	662	13.1	5.0
10	Rødsand II	ERA5	9.1	761	17.2	3.7
		NORA3	9.4	646	12.8	5.0
11	Kriegers Flak	ERA5	9.7	691	16.0	3.8
		NORA3	9.6	576	11.8	5.3
12	EnBW Baltic	ERA5	8.7	663	14.7	4.8
		NORA3	9.4	589	12.0	5.2
13	Bornholm	ERA5	9.7	689	15.8	3.9
		NORA3	9.7	580	11.7	5.2
Offshore Averages		ERA5	9.4	715	16.3	3.9
		NORA3	9.5	622	12.5	5.0
		Rel. bias	-0.9%	15.0%	30.3%	-21.9%

of its kind, there are no existing maps to directly compare the general patterns of the erosion onset time results. Nonetheless, related research [17,7,11,13] has been conducted on blade coating lifetimes and incubation periods in specific locations also covered by our atlas. These studies consistently indicate that the predicted lifetimes or incubation periods tend to be shorter in coastal and offshore regions, aligning with the findings of our research.

Our comparative analysis with actual measurements indicates that the NORA3 rain field predictions align more accurately with observed rainfall than those from ERA5 at both measurement sites. This is evident both in the frequency domain (as shown in Fig. 3) and in terms of cumulative rainfall (illustrated in Fig. 4). This finding is consistent with

prior research [30–33] identifying a wet bias in the ERA5 rainfall. The relative lack of high-frequency energy content in ERA5 rain predictions, coupled with its overall higher cumulative rainfall, leads to a temporal ‘smearing’ of rain events in the model, resulting in more frequent but less intense rain events.

The discrepancies between the rain predictions of these models significantly influence the modeled damage progression (as depicted in Fig. 4). It is observed that the cumulative damage progression generally mirrors the pattern of cumulative rainfall. However, there is a notable exception in the damage progression based on measurements at Thyborøn (Fig. 4 d)), which stands out as an anomaly, due to the differences in wind speed. The measured wind speeds at Thyborøn are affected by

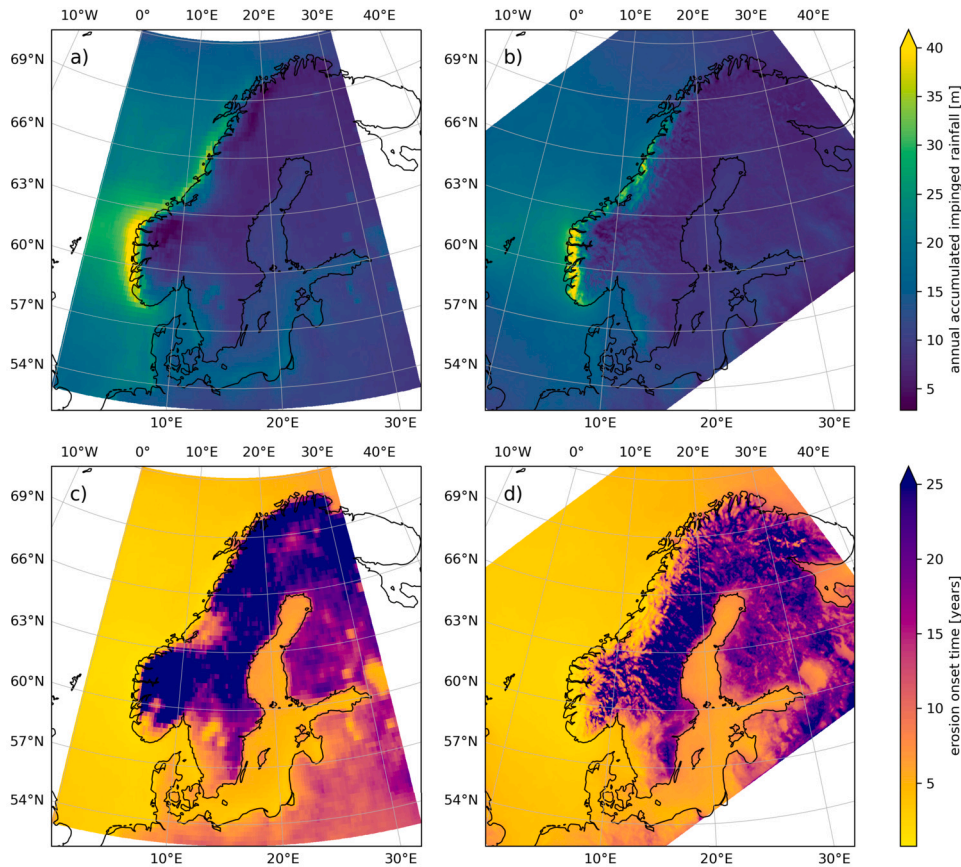


Fig. 6. The annual accumulated impinged rainfall for a) ERA5, b) NORA3 and the onset time of erosion for c) ERA5 and d) NORA3. The layers are calculated for the IEA 15 MW wind turbine (all panels) and a commercial blade material (lower panels).

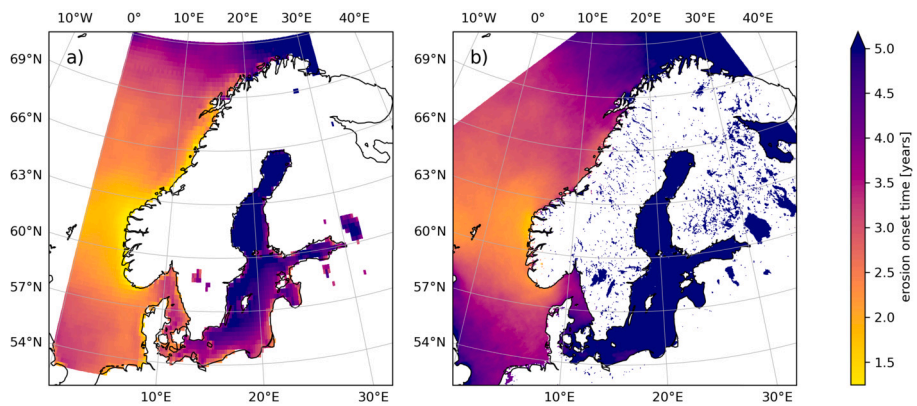


Fig. 7. The onset time of rain erosion for a) ERA5 and b) NORA3 for sea areas. The layers are calculated for the IEA 15 MW wind turbine and a commercial blade material.

nearby structures and obstacles, and although these speeds have been extrapolated using the power law, they occasionally approach 0 m/s. In contrast, the modeled wind speeds are not influenced by these obstacles and are therefore higher on average and do not include prolonged periods below the cut-in wind speed of the reference wind turbine.

The maps of annual average wind speed in Fig. 2 show a notable difference between the modeled wind speed in the mountainous area of Norway, where the ERA5 wind speed is significantly lower. This difference aligns with a number of studies that have shown that the ERA5 wind speed is underestimated in mountainous terrain [24,34,35]. Several factors likely contribute to the underestimation of ERA5 wind speeds in mountainous terrain. Firstly, the low spatial resolution of ERA5 is insufficient to model the acceleration of winds over hill- and

mountain tops, i.e. the orographic speed up effect is under-resolved. Secondly, the representation of orographic drag processes, recognized as a significant source of uncertainty in numerical weather prediction models [36], leads to too high drag over mountainous areas in ERA5. Lastly, the hydrostatic model formulation of ERA5 neglects vertical acceleration, which limits the simulated wind flow over the mountains. This differs from the non-hydrostatic dynamics used in NORA3.

Given the well-established tendency of ERA5 to underestimate wind speeds onshore, particularly in complex terrain [24,34,35], a notable difference was expected between the erosion layer results of NORA3 and ERA5 in the onshore areas. Conversely, the results for offshore areas were expected to be more aligned. This expectation is largely confirmed in our findings, as illustrated in Fig. 6 and Fig. 7, where the offshore

results are indeed more consistent. However, it's noteworthy that the incubation times in these offshore areas are significantly lower for the predictions based on ERA5, as detailed in Tables 2 and 3. The primary reason for this discrepancy appears to be the wet bias present in the ERA5 dataset since the mean offshore winds from both models are more similar (low relative bias in Tables 2 and 3).

In the erosion onset time map derived from ERA5 data (Fig. 6 c), we observe a pronounced increase in erosion risk along the western coasts, indicated by shorter incubation times. This pattern is likely a consequence of the limited spatial resolution of the ERA5 model, which does not adequately resolve coastal features. As a result, the influence of the coastline, such as changes in surface roughness and elevation, is overextended into offshore areas, impacting both wind fields and precipitation patterns. In contrast, the NORA3 rain erosion map (Fig. 6 d) reveals that the highest erosion risk is located inland on the west coast of Norway. Despite NORA3 being a modeled dataset with its own set of errors, the substantially higher spatial resolution provides more reliable results, as elaborated in Section 2.4.

The damage model employed in our atlas is founded on rain erosion tests and is specifically designed to predict the onset of erosion due to liquid precipitation only. This means our results exclusively consider erosion due to rain, without accounting for other erosive factors like hail, wet snow, UV radiation, and sandstorms [1]. Nevertheless, within the scope of our study, which focuses on Scandinavia, rain is presumed to be the predominant factor contributing to leading-edge erosion damages, although further research may be needed to conclusively confirm this assumption.

Unlike a wind atlas, a rain erosion atlas is essentially linked to specific wind turbine characteristics. A wind atlas is based on wind data and the wind resource and energy density are calculated without information about a specific wind turbine. Thus energy density is a turbine-agnostic metric. In contrast, rain erosion is related to the impinged water at the specific blade. Thus, the rain erosion atlas is valid for specific turbine parameters with the key information of the blade tip speed. To predict the damage progression and blade lifetime, it is necessary to have information on the VH curve from the rain erosion test for the specific coating material. Using a VH curve for a more durable coating material would lead to longer erosion onset times for our results. We would also increase the incubation times by using reference turbine models for smaller turbines, e.g. a 10 MW or a 5 MW turbines that operate at lower heights with lower speeds and have shorter blades leading to lower maximum tip speeds. It should also be noted that the onset time of erosion only marks the initial signs of erosion, differing from the overall blade lifetime which indicates a more severe stage of erosion requiring blade repair. Therefore, repair interventions would occur significantly later than the initial onset of erosion.

5. Conclusion

In this study, we have demonstrated a framework that can effectively identify areas prone to erosion due to liquid precipitation. This marks the first creation of a rain erosion atlas for the Scandinavian region including Denmark and Finland. We compared the results derived from ERA5 and NORA3 with those derived from weather station measurements at Utsira in Norway and Thyborøn in Denmark. It is evident that NORA3 data correspond more closely with the actual measurements across various parameters, including power spectral density, mean wind speed, annual accumulated rainfall, and the predicted rain erosion damage.

The findings from the Scandinavian rain erosion atlas can be summarized as follows:

- Areas characterized by high precipitation combined with high wind speed exhibit shorter erosion onset times;
- Offshore areas are identified as critical for rain erosion, with the southwest coast of Norway being the most critical area;

- Results at selected wind farm location in the North Sea, the onset time of erosion is on average 3.2 years and 5 years in the Baltic sea, based on NORA3 data;
- Based on NORA3 data, the onset time of erosion is on average 5 years for Baltic Sea wind farm sites and 3.2 years for North Sea sites

Our findings reveal that the ERA5 model overestimates rain at all analyzed wind farm locations with a relative bias of 20% at North Sea and Norwegian Sea locations and 15% at the inner Danish Seas and Baltic Sea. The wind speed bias is generally low, less than -1%. This discrepancy leads to an underestimation of the onset time of erosion based on ERA5, where the relative bias is -24% at North Sea and Norwegian Sea locations and -22% at the inner Danish Seas and Baltic Sea.

Our research highlights the importance of considering both wind and rain parameters in assessing erosion risk. The differences in model performance underscore the need for utilizing high-resolution data, like that from NORA3, for more accurate predictions, especially in coastal and offshore areas. This study lays the groundwork for future research in this field and offers valuable insights for the wind energy sector, particularly in optimizing turbine design and maintenance strategies in erosion-prone regions.

CRedit authorship contribution statement

Ásta Hannesdóttir: Writing – original draft, Writing – review & editing, Visualization, Validation, Software, Methodology, Investigation, Funding acquisition, Formal analysis, Data curation, Conceptualization. **Stephan T. Kral:** Writing – original draft, Writing – review & editing, Visualization, Validation, Software, Methodology, Investigation, Data curation, Conceptualization. **Joachim Reuder:** Writing – original draft, Writing – review & editing, Methodology, Investigation, Funding acquisition, Conceptualization. **Charlotte Bay Hasager:** Writing – original draft, Writing – review & editing, Investigation, Funding acquisition, Formal analysis, Conceptualization.

Declaration of competing interest

The authors confirm that there are no competing financial interests or personal relationships that might be perceived to have influenced the findings presented in this paper.

Data availability

The python code used to calculate the atlas layers, data with calculated atlas layers, and a python script for plotting is available at: https://gitlab.windenergy.dtu.dk/astah/era5_erosion_atlas.

Acknowledgement

This research was supported by the project “Estimation and Prevention of Erosion on Off-Shore Wind Turbine Blades” (102235103) funded by the Academia Agreement between the University of Bergen and Equinor. Authors Hannesdóttir and Hasager acknowledge the partial support of the IEA task 46 “Erosion of wind turbine blades” EUDP grant J.nr. 64021-0003 and the project HORIZON Europe Grant “AIRE” (101083716).

We acknowledge the ECMWF for the ERA5 data, the Norwegian Meteorological Institute for the Utsira Fyr measurements and the NORA3 data, and the Danish Meteorological Institute for the measurements at Thyborøn.

References

- [1] W. Han, J. Kim, B. Kim, Effects of contamination and erosion at the leading edge of blade tip airfoils on the annual energy production of wind turbines, *Renew. Energy* 115 (2018) 817–823, <https://doi.org/10.1016/j.renene.2017.09.002>.

- [2] M.H. Keegan, D.H. Nash, M.M. Stack, On erosion issues associated with the leading edge of wind turbine blades, *J. Phys. D, Appl. Phys.* 46 (38) (2013) 383001, <https://doi.org/10.1088/0022-3727/46/38/383001>.
- [3] L. Mishnaevsky, K. Thomsen, Costs of repair of wind turbine blades: influence of technology aspects, *Wind Energy* 23 (12) (2020) 2247–2255, <https://doi.org/10.1002/we.2552>.
- [4] L. Mishnaevsky, C.B. Hasager, C. Bak, A.M. Tilg, J.I. Bech, S. Doagov Rad, S. Fæster, Leading edge erosion of wind turbine blades: understanding, prevention and protection, *Renew. Energy* 169 (2021) 953–969, <https://doi.org/10.1016/j.renene.2021.01.044>.
- [5] S.C. Pryor, R.J. Barthelmie, J. Cadence, E. Dellwik, C.B. Hasager, S.T. Kral, J. Reuder, M. Rodgers, M. Veraart, Atmospheric drivers of wind turbine blade leading edge erosion: review and recommendations for future research, *Energies* 15 (22) (2022) 8553, <https://doi.org/10.3390/en15228553>.
- [6] DNVGL-RP-0171, Testing of Rotor Blade Erosion Protection Systems, Recommended practice, DNV GL, Oslo, Norway (2018).
- [7] J.I. Bech, N.F.J. Johansen, M.B. Madsen, Á. Hannesdóttir, C.B. Hasager, Experimental study on the effect of drop size in rain erosion test and on lifetime prediction of wind turbine blades, *Renew. Energy* 197 (2022) 776–789, <https://doi.org/10.1016/j.renene.2022.06.127>.
- [8] R. Prieto, T. Karlsson, A model to estimate the effect of variables causing erosion in wind turbine blades, *Wind Energy* 24 (9) (2021) 1031–1044, <https://doi.org/10.1002/we.2615>.
- [9] J. Visbeck, T. Göçmen, C.B. Hasager, H. Shkalov, M. Handberg, K.P. Nielsen, Introducing a data-driven approach to predict site-specific leading-edge erosion from mesoscale weather simulations, *Wind Energy Sci.* 8 (2) (2023) 173–191, <https://doi.org/10.5194/wes-8-173-2023>.
- [10] D. Eisenberg, S. Laustsen, J. Stege, Wind turbine blade coating leading edge rain erosion model: development and validation, *Wind Energy* 21 (10) (2018) 942–951, <https://doi.org/10.1002/we.2200>.
- [11] C. Hasager, F. Vejen, J.I. Bech, W.R. Skrzypiąski, A.M. Tilg, M. Nielsen, Assessment of the rain and wind climate with focus on wind turbine blade leading edge erosion rate and expected lifetime in Danish Seas, *Renew. Energy* 149 (2020) 91–102, <https://doi.org/10.1016/j.renene.2019.12.043>.
- [12] C.B. Hasager, F. Vejen, W.R. Skrzypiąski, A.-M. Tilg, Rain erosion load and its effect on leading-edge lifetime and potential of erosion-safe mode at wind turbines in the North Sea and Baltic Sea, *Energies* 14 (7) (2021) 1959, <https://doi.org/10.3390/en14071959>.
- [13] A.S. Verma, Z. Jiang, M. Caboni, H. Verhoef, H. van der Mijle Meijer, S.G. Castro, J.J. Teuwen, A probabilistic rainfall model to estimate the leading-edge lifetime of wind turbine blade coating system, *Renew. Energy* 178 (2021) 1435–1455, <https://doi.org/10.1016/j.renene.2021.06.122>.
- [14] A.S. Verma, Z. Jiang, Z. Ren, M. Caboni, H. Verhoef, H. Mijle-Meijer, S.G. Castro, J.J. Teuwen, A probabilistic long-term framework for site-specific erosion analysis of wind turbine blades: a case study of 31 Dutch sites, *Wind Energy* 24 (11) (2021) 1315–1336, <https://doi.org/10.1002/we.2634>.
- [15] F. Letson, R.J. Barthelmie, S.C. Pryor, Radar-derived precipitation climatology for wind turbine blade leading edge erosion, *Wind Energy Sci.* 5 (1) (2020) 331–347, <https://doi.org/10.5194/wes-5-331-2020>.
- [16] H. Punge, K. Bedka, M. Kunz, A. Reinbold, Hail frequency estimation across Europe based on a combination of overshooting top detections and the ERA-INTERIM reanalysis, *Atmos. Res.* 198 (June 2017) 34–43, <https://doi.org/10.1016/j.atmosres.2017.07.025>.
- [17] M. Badger, H. Zuo, Á. Hannesdóttir, A. Owda, C. Hasager, Lifetime prediction of turbine blades using global precipitation products from satellites, *Wind Energy Sci.* 7 (6) (2022) 2497–2512, <https://doi.org/10.5194/wes-7-2497-2022>.
- [18] N. Mortensen, J. Hansen, M. Kelly, E. Prinsloo, E. Mabilile, S. Szewczuk, *Wind Atlas for South Africa (WASA) Station and Site Description Report*, 2012.
- [19] N. Nawri, G. Petersen, H. Björnsson, A. Hahmann, K. Jónasson, C. Hasager, N.-E. Clausen, The wind energy potential of Iceland, *Renew. Energy* 69 (2014) 290–299, <https://doi.org/10.1016/j.renene.2014.03.040>, this is an open access article under the CC BY-NC-ND license.
- [20] A.N. Hahmann, T. Sile, B. Witha, N.N. Davis, M. Dörenkämper, Y. Ezber, E. García-Bustamante, J.F. González-Rouco, J. Navarro, B.T. Olsen, S. Söderberg, The making of the new European wind atlas – Part 1: model sensitivity, *Geosci. Model Dev.* 13 (10) (2020) 5053–5078, <https://doi.org/10.5194/gmd-13-5053-2020>, <https://gmd.copernicus.org/articles/13/5053/2020/>.
- [21] N. Davis, J. Badger, A. Hahmann, B. Hansen, N. Mortensen, M. Kelly, X. Larsén, B. Olsen, R. Floors, G. Lizcano, P. Casso, O. Lacave, A. Bosch, I. Bauwens, O. Knight, A. Loon, R. Fox, T. Parvanyan, S. Hansen, D. Heathfield, M. Onninen, R. Drummond, The global wind atlas: a high-resolution dataset of climatologies and associated web-based application, *Bull. Am. Meteorol. Soc.* 104 (8) (2023) E1507–E1525, <https://doi.org/10.1175/BAMS-D-21-0075.1>.
- [22] X.G. Larsén, N. Davis, Á. Hannesdóttir, M. Kelly, L. Svenningsen, R. Slot, M. Imberger, B.T. Olsen, R. Floors, The global atlas for siting parameters project: extreme wind, turbulence, and turbine classes, *Wind Energy* 25 (11) (2022) 1841–1859, <https://doi.org/10.1002/we.2771>, <https://onlinelibrary.wiley.com/doi/pdf/10.1002/we.2771>, <https://onlinelibrary.wiley.com/doi/abs/10.1002/we.2771>.
- [23] H. Hershbach, B. Bell, P. Berrisford, S. Hirahara, A. Horányi, J. Muñoz-Sabater, J. Nicolas, C. Peubey, R. Radu, D. Schepers, A. Simmons, C. Soci, S. Abdalla, X. Abellan, G. Balsamo, P. Bechtold, G. Biavati, J. Bidlot, M. Bonavita, G. Chiara, P. Dahlgren, D. Dee, M. Diamantakis, R. Dragani, J. Flemming, R. Forbes, M. Fuentes, A. Geer, L. Haimberger, S. Healy, R.J. Hogan, E. Hólm, M. Janisková, S. Keeley, P. Laloyaux, P. Lopez, C. Lupu, G. Radnoti, P. Rosnay, I. Rozum, F. Vamborg, S. Villaume, J. Thépaut, The ERA5 global reanalysis, *Q. J. R. Meteorol. Soc.* 146 (730) (2020) 1999–2049, <https://doi.org/10.1002/qj.3803>.
- [24] H. Haakenstad, Ø. Breivik, B.R. Furevik, M. Reistad, P. Böhlinger, O.J. Aarnes, NORAS: a nonhydrostatic high-resolution hindcast of the North Sea, the Norwegian Sea, and the Barents Sea, *J. Appl. Meteorol. Climatol.* 60 (10) (2021) 1443–1464, <https://doi.org/10.1175/JAMC-D-21-0029.1>.
- [25] A.C. Best, The size distribution of raindrops, *Q. J. R. Meteorol. Soc.* 76 (327) (1950) 16–36, <https://doi.org/10.1002/qj.49707632704>.
- [26] E. Gaertner, J. Rinker, L. Sethuraman, F. Zahle, B. Anderson, G. Barter, N. Abbas, F. Meng, P. Bortolotti, W. Skrzypinski, G. Scott, R. Feil, H. Bredmose, K. Dykes, M. Shields, C. Allen, A. Viselli, Definition of the IEA Wind 15-Megawatt Offshore Reference Wind Turbine, Technical Report, Tech. Rep., 2020.
- [27] H. Slot, E. Gelinck, C. Rentrop, E. van der Heide, Leading edge erosion of coated wind turbine blades: review of coating life models, *Renew. Energy* 80 (2015) 837–848, <https://doi.org/10.1016/j.renene.2015.02.036>.
- [28] A. Peña, T. Mikkelsen, S.-E. Gryning, C. Hasager, A. Hahmann, M. Badger, I. Karagali, M. Courtney, Offshore vertical wind shear: Final report on NORSEWind's work task 3.11, no. 0005 in DTU Wind Energy E, DTU Wind Energy, Denmark, 2012.
- [29] A. Peña, R. Floors, A. Sathe, S.-E. Gryning, R. Wagner, M. Courtney, X. Larsén, A. Hahmann, C. Hasager, Ten years of boundary-layer and wind-power meteorology at Høvsøre, Denmark, *Bound.-Layer Meteorol.* 158 (1) (2016) 1–26, <https://doi.org/10.1007/s10546-015-0079-8>.
- [30] D.A. Lavers, A. Simmons, F. Vamborg, M.J. Rodwell, An evaluation of ERA5 precipitation for climate monitoring, *Q. J. R. Meteorol. Soc.* 148 (748) (2022) 3152–3165, <https://doi.org/10.1002/qj.4351>.
- [31] Q. Jiang, W. Li, Z. Fan, X. He, W. Sun, S. Chen, J. Wen, J. Gao, J. Wang, Evaluation of the ERA5 reanalysis precipitation dataset over Chinese Mainland, *J. Hydrol.* 595 (10) (2021) 125660, <https://doi.org/10.1016/j.jhydrol.2020.125660>.
- [32] D. Jiao, N. Xu, F. Yang, K. Xu, Evaluation of spatial-temporal variation performance of ERA5 precipitation data in China, *Sci. Rep.* 11 (1) (2021) 17956, <https://doi.org/10.1038/s41598-021-97432-y>.
- [33] M. Bandhauer, F. Isotta, M. Lakatos, C. Lussana, L. Båserud, B. Izsák, O. Szentés, O.E. Tveito, C. Frei, Evaluation of daily precipitation analyses in E-OBS (v19.0e) and ERA5 by comparison to regional high-resolution datasets in European regions, *Int. J. Climatol.* 42 (2) (2022) 727–747, <https://doi.org/10.1002/joc.7269>.
- [34] B. Jourdiere, Evaluation of ERA5, MERRA-2, COSMO-REA6, NEWA and AROME to simulate wind power production over France, *Adv. Appl. Sci. Res.* 17 (2020) 63–77, <https://doi.org/10.5194/asr-17-63-2020>.
- [35] M. Dörenkämper, B.T. Olsen, B. Witha, A.N. Hahmann, N.N. Davis, J. Barcons, Y. Ezber, E. García-Bustamante, J.F. González-Rouco, J. Navarro, M. Sastre-Marugán, T. Sile, W. Trei, M. Žagar, J. Badger, J. Gottschall, J. Sanz Rodrigo, J. Mann, The making of the new European wind atlas – Part 2: production and evaluation, *Geosci. Model Dev.* 13 (10) (2020) 5079–5102, <https://doi.org/10.5194/gmd-13-5079-2020>, <https://gmd.copernicus.org/articles/13/5079/2020/>.
- [36] I. Sandu, A. Zadra, N. Wedi, Impact of orographic drag on forecast skill (2017 2017), <https://doi.org/10.21957/icghjbyln7>, <https://www.ecmwf.int/node/18163>.